

UNCLASSIFIED

AD NUMBER
ADB231930
NEW LIMITATION CHANGE
TO Approved for public release, distribution unlimited
FROM Distribution authorized to U.S. Gov't. agencies only; Specific Authority; 11 Dec 97. Other requests shall be referred to US Army Medical Research and Materiel Comd., ATTN: MCMR-RMI-S. Fort Detrick, MD 21702-5012.
AUTHORITY
USAMRMC ltr, 4 Dec 2003

THIS PAGE IS UNCLASSIFIED

AD _____

CONTRACT NUMBER DAMD17-95-C-5033

TITLE: An Acoustic Plate Mode Sensor for Biowarfare Toxins

PRINCIPAL INVESTIGATOR: Douglas J. McAllister, Ph.D.

CONTRACTING ORGANIZATION: Biode, Incorporated
Bangor, Maine 04401

REPORT DATE: October 1997

TYPE OF REPORT: Annual, Phase II

PREPARED FOR: U.S. Army Medical Research and Materiel Command
Fort Detrick, Maryland 21702-5012

DISTRIBUTION STATEMENT: Distribution authorized to U.S. Government agencies only (specific authority). Other requests for this document shall be referred to U.S. Army Medical Research and Materiel Command, Fort Detrick, Maryland 21702-5012 (ATTN: MCMR-RMI-S).

The views, opinions and/or findings contained in this report are those of the author(s) and should not be construed as an official Department of the Army position, policy or decision unless so designated by other documentation.

DTIC QUALITY INSPECTED 2

19971210 102

REPORT DOCUMENTATION PAGE

Form Approved
OMB No. 0704-0188

Public reporting burden for this collection of information is estimated to average 1 hour per response, including the time for reviewing instructions, searching existing data sources, gathering and maintaining the data needed, and completing and reviewing the collection of information. Send comments regarding this burden estimate or any other aspect of this collection of information, including suggestions for reducing this burden, to Washington Headquarters Services, Directorate for Information Operations and Reports, 1215 Jefferson Davis Highway, Suite 1204, Arlington, VA 22202-4302, and to the Office of Management and Budget, Paperwork Reduction Project (0704-0188), Washington, DC 20503.

1. AGENCY USE ONLY (Leave blank)		2. REPORT DATE October 1997		3. REPORT TYPE AND DATES COVERED Annual-Phase II (1 Aug 96 - 31 Jul 97)	
4. TITLE AND SUBTITLE An Acoustic Plate Mode Sensor for Biowarfare Toxins				5. FUNDING NUMBERS DAMD17-95-C-5033	
6. AUTHOR(S) Douglas J. McAllister, Ph.D.					
7. PERFORMING ORGANIZATION NAME(S) AND ADDRESS(ES) Biode, Incorporated Bangor, Maine 04401				8. PERFORMING ORGANIZATION REPORT NUMBER 96-02-FY1	
9. SPONSORING/MONITORING AGENCY NAME(S) AND ADDRESS(ES) Commander U.S. Army Medical Research and Materiel Command Fort Detrick, Frederick, Maryland 21702-5012				10. SPONSORING/MONITORING AGENCY REPORT NUMBER	
11. SUPPLEMENTARY NOTES					
12a. DISTRIBUTION / AVAILABILITY STATEMENT Distribution authorized to U.S. Government agencies only (specific authority). Other requests for this document shall be referred to United States Army Medical Research and Materiel Command, 504 Scott Street, Fort Detrick, Maryland 21702-5012, ATTN: MCMR-RMT-S.				12b. DISTRIBUTION CODE	
13. ABSTRACT (Maximum 200) This report details the design, evaluation and experimental data obtained during the first fiscal year of the contract. Results are presented in five areas. (1) The covalent attachment of immunoglobulin G (IgG) to gold surfaces and the supporting surface chemical analysis; (2) the design and evaluation of the piezoelectric sensors; (3) the design and evaluation of the measurement electronics; (4) the design and construction of a microprocessor-based user interface; and (5) the discussion of preliminary biosensor data. A stable and reusable attachment procedure is obtained using poly-(propylmercapto methyl siloxane) and thioalkylated antibody, which yields a 0.8 to 1.5 ng/mm ² binding. Acoustic plate mode and thickness shear mode sensors have been designed. Surface transverse wave devices offer higher sensitivity; however, further engineering effort is required. Sensitivity of 0.75x10 ⁻⁶ to 1.4x10 ⁻⁶ mm ² /ng and resolution of 0.25x10 ⁻⁶ is observed. Two measurement systems have been designed and tested. Microprocessor system development is ahead of schedule. Preliminary biosensor data is offered using Y. Pestis. The data indicates marginal detection, consistent with a sensitivity to resolution ratio of 3:1. Improvements are suggested for FY2 effort.					
14. SUBJECT TERMS Acoustic Plate Mode, Biowarfare Toxins				15. NUMBER OF PAGES 54	
				16. PRICE CODE	
17. SECURITY CLASSIFICATION OF REPORT Unclassified	18. SECURITY CLASSIFICATION OF THIS PAGE Unclassified	19. SECURITY CLASSIFICATION OF ABSTRACT Unclassified	20. LIMITATION OF ABSTRACT Limited		

FOREWORD

Opinions, interpretations, conclusions and recommendations are those of the author and are not necessarily endorsed by the U.S. Army.

____ Where copyrighted material is quoted, permission has been obtained to use such material.

____ Where material from documents designated for limited distribution is quoted, permission has been obtained to use the material.

CA Citations of commercial organizations and trade names in this report do not constitute an official Department of Army endorsement or approval of the products or services of these organizations.

____ In conducting research using animals, the investigator(s) adhered to the "Guide for the Care and Use of Laboratory Animals," prepared by the Committee on Care and Use of Laboratory Animals of the Institute of Laboratory Resources, National Research Council (NIH Publication No. 86-23; Revised 1985).

____ For the protection of human subjects, the investigator(s) adhered to policies of applicable Federal Law 45 CFR 46.

____ In conducting research utilizing recombinant DNA technology, the investigator(s) adhered to current guidelines promulgated by the National Institutes of Health.

____ In the conduct of research utilizing recombinant DNA, the investigator(s) adhered to the NIH Guidelines for Research Involving Recombinant DNA Molecules.

____ In the conduct of research involving hazardous organisms, the investigator(s) adhered to the CDC-NIH Guide for Biosafety in Microbiological and Biomedical Laboratories.

Douglas J. McAllister
PI - Signature _____ Date

II) Table of Contents

I) FOREWORD	3
II) TABLE OF CONTENTS.....	4
I) INTRODUCTION	6
II) BODY	7
II.A) IMMOBILIZATION CHEMISTRY	7
II.A.1) <i>Scope and Schedule. Extensions to Scope</i>	7
II.A.2) <i>Thiol-Gold Biochemistry</i>	7
II.A.3) <i>Regeneration and Storage</i>	10
II.A.4) <i>Strip and Reuse</i>	13
II.A.5) <i>Antibody Selectivity (from DAAM01-95C-0076)</i>	13
II.A.6) <i>Radiolabeled Antibody Studies</i>	13
II.A.7) <i>Thiol-Gold Surface Chemistry</i>	15
II.A.7.a) <i>Preliminary Effort and Implications</i>	15
II.A.7.b) <i>Further Electrochemical Studies</i>	16
II.B) PIEZOELECTRIC SENSORS.....	17
II.B.1) <i>Scope and Schedule. Extensions to Scope</i>	17
II.B.2) <i>Overview of Shear Wave Piezoelectric Sensor Geometries</i>	18
II.B.3) <i>Quartz SHAPM (from parallel project: DE-FG02-94ER-81717)</i>	22
II.B.3.a) <i>Pure SH Acoustic Plate Modes, AT-90 Quartz</i>	22
II.B.3.b) <i>Description of Modes In Rotated Y-cut X-propagating APM Spectra</i>	23
II.B.3.c) <i>The Slow Shear Bulk Wave for X-propagating Rotated Y-Cut</i>	24
II.B.3.d) <i>Acoustic Plate Modes Based on Compressional Bulk Waves</i>	25
II.B.3.e) <i>Acoustic Plate Modes Based on the Fast Shear Bulk Wave</i>	26
II.B.3.f) <i>Summary of APMs Derived from Specific Bulk Acoustic Waves</i>	26
II.B.3.g) <i>APMs Derived from an Independent Leaky SAW</i>	26
II.B.4) <i>Lithium Tantalate Shear Horizontal Acoustic Plate Mode (SHAPM)</i>	28
II.B.4.a) <i>Approach for the Orientation Search</i>	28
II.B.4.b) <i>Generalized Rotated Y-cut (RYC) Orientation Search</i>	28
II.B.4.c) <i>Generalized Rotated X-cut (RXC) Orientation Search</i>	30
II.B.4.d) <i>Generalized Rotated YX-cut (RYXC) Orientation Search</i>	30
II.B.4.e) <i>Modeling of Candidate Devices</i>	30
II.B.4.f) <i>Measurement of Prototype Devices</i>	31
II.B.5) <i>Quartz STW (partially supported by DAAM01-95C-0076)</i>	32
II.B.6) <i>Lithium Tantalate Surface Transverse Wave (STW)</i>	40
II.B.7) <i>Quartz Monolithic Piezoelectric Sensor (MPS)</i>	40
II.C) MEASUREMENT ELECTRONICS.....	43

II.C.1) <i>Scope and Schedule. Extensions to Scope</i>	43
II.C.2) <i>Oscillator Electronics</i>	43
II.C.3) <i>Phase Interferometry</i>	43
II.C.4) <i>Support Electronics (Frequency Counters, Frequency Prescalers, Temperature Measurement and Electrochemical Control)</i>	45
II.D) PACKAGING AND USER INTERFACE	46
II.D.1) <i>Introduction</i>	46
II.D.2) <i>Microcontroller</i>	46
II.D.2.a) <i>Main system overview and code/system information</i>	46
II.D.2.b) <i>Liquid crystal display (LCD) overview</i>	47
II.D.2.c) <i>Keypad/encoder overview</i>	47
II.D.2.d) <i>Waveform/digital-analog converter overview</i>	47
II.D.2.e) <i>Serial communication overview</i>	48
II.D.2.f) <i>Differential frequency counter (DFC) overview</i>	48
II.E) CHARACTERIZE THE PHASE II PROTOTYPES (DATA FROM DAAM01-95C-0076)	49
II.F) PROJECT STATUS FOR FY1 AND RECOMMENDED RESEARCH AND DEVELOPMENT FOR FY2	50
II.F.1) <i>Current Status of Attachment Chemistry</i>	50
II.F.1.a) <i>Perform electrochemical tests on PMS films with $\text{Fe}(\text{CN})_6^{-3}$</i>	50
II.F.1.b) <i>Continue longevity tests</i>	50
II.F.1.c) <i>Perform thiodialkyne longevity / regeneration test</i>	50
II.F.1.d) <i>Perform initial study of thioalkene process</i>	50
II.F.1.e) <i>Perform initial study of electrochemical biochemistry</i>	50
II.F.2) <i>Status and Recommendations for the Piezoelectric Sensor</i>	50
II.F.2.a) <i>SHAPM Devices</i>	51
II.F.2.b) <i>STW Devices</i>	51
II.F.2.c) <i>MPS Devices</i>	51
II.F.3) <i>Status of the Measurement Electronics</i>	51
II.F.4) <i>Status of the Microcontroller</i>	52
II.F.5) <i>Biosensor Measurements</i>	52
III) REFERENCES	52

D) Introduction

Military personnel are vulnerable to many chemical and biological agents in the field. Biological agents -- such as bacteria, bacterial toxins and viruses -- must be detected rapidly to allow their neutralization or the quick treatment of infected personnel. These agents may be detected using either immunological (antibody-antigen) or genomic (DNA) diagnostics. These tests are typically performed using enzyme-linked immunosorbent assay (ELISA), latex bead agglutination kits or radio-labeled probes. All of these diagnostic techniques are capable of nanogram per milliliter detection; however, they all require multiple incubations, careful washes and well-trained technicians. Ideally, a soldier should be able to administer the required test -- in a single step -- in the field with immediate (a few minutes) feedback. The ability to analyze a single biological sample (e.g. a drop of blood) for a variety of biowarfare agents is highly desirable.

One approach - which currently allows the rapid (<5 minutes) detection of minute quantities (~10 ng/ml) of antigen, antibody or DNA - employs a piezoelectric biosensor (array) for the immunological or genomic detection of the target biochemical agent. Piezoelectric acoustic wave sensors are solid state devices that are highly sensitive to minute mass and / or electrical changes at their boundaries. The piezoelectric sensors use acoustic waves to probe an adjacent biochemical solution. These waves are excited and received by metal electrodes that have been deposited on the surface of the piezoelectric crystal. A number of highly sensitive piezoelectric biosensors have been proposed [1] which are capable of being operated directly in solution. The most promising of those in the literature are the quartz crystal microbalance (QCM), the shear horizontal acoustic plate mode (SHAPM) and surface transverse wave (STW) sensors. Lamb wave sensors have also been shown to have excellent sensitivity but are not suitably rugged for most applications. Shear horizontal acoustic plate mode (SHAPM) biosensors have been proposed for various fluid-phase sensing applications, including ionic strength determination [2], measurement of viscosity [3], selective detection of metals [3] and biochemical detection [4].

Piezoelectric sensors detect analyte via mechanical or electrical perturbations at or near the surface of a piezoelectric crystal. Fluid phase devices typically employ a shear wave with minimal evanescent penetration into the bulk [1]. Biosensors almost exclusively employ mechanical perturbations. Perturbations to the acoustic wave during biochemical recognition events (e.g. antibody-antigen binding) cause the wave velocity to decrease, which typically increases the phase shift through the device. This phase shift may be directly measured using a phase bridge. Alternately, an oscillator circuit may be employed to transduce the phase shifts to a more easily measured frequency shift, since the circuit responds to phase perturbations by reducing the oscillation frequency to compensate for the additional phase shift. In a mass based piezoelectric sensor, the frequency shift is directly proportional to the bound mass per unit area. Therefore, the response is often described as an effective mass sensitivity that relates the response to the complex perturbation. Other properties affecting response include changes in wetting of the surface, the volume of viscously entrained liquids, film stiffness and actual mass. Mass is the dominant perturbation for globular proteins while changes in the quantity of viscously coupled fluid are also significant for DNA [5] and improve the sensitivity three to four-fold.

II) Body

II.A) Immobilization Chemistry

II.A.1) Scope and Schedule. Extensions to Scope.

The proposed effort detailed a study of thioalkane and thio-dialkynes cross-linking agents. Thioalkanes, typified by mercaptoundecanoic acid (MUA) and hexadecylthiol (HDT), have been studied and were found to exhibit poor stability over thermal, electrochemical and chemical extremes. Related compounds containing a conjugated triple bond internal to the alkane section exhibited excellent stability. Unfortunately, synthesis of these compounds is tedious and inefficient. The shelf life of these compounds is short, making it necessary to continuously synthesize and purify reagents as needed. Thus, the effort on attachment chemistry has been expanded to consider other thiol-gold interactions, such as polymercaptopropyl methyl siloxane (PMS). While the thio-dialkynes are, in principle, technically superior to PMS, PMS is extremely stable and readily available.

Research into the biochemical attachment was scheduled for completion in FY1. The contract goals have been met on schedule; however, improving binding capacity is essential to the optimal performance of the sensor. BIODE proposes to continue research into the attachment process during FY2 as a low-level, background task. Specifically, three tasks will be continued:

- 1) Continue longevity / storage studies on PMS.
- 2) Examine thioalkenes as a synthesis route to polyethylene oxide / antibody surfaces.
- 3) Examine the effects of electrochemical bias on binding capacity.

These tasks are discussed in the FY2 effort section, below. The following sections detail representative experiments on the attachment of antibody to gold films.

II.A.2) Thiol-Gold Biochemistry)

An increase in the binding capacity of antibody to gold is desired in order to provide a lower detection limit for the sensor. Poly (mercaptopropyl methyl siloxane) (PMS) / thioalkylated N-succinimidyl 3-(2-pyridyldithio) propionate (SPDP'd) antibody procedure has been compared to other methods based on hydrophobic / hydrophilic interactions, other siloxanes and silanes and to thioalkane self assembled monolayers (SAM). Most of these techniques employ acid (COOH) functionalized surfaces in a condensation reaction with amino functionals on the antibody. 1-ethyl 3-(3-dimethyl aminopropyl) carbodiimide (EDC) was employed to promote this condensation reaction. The antigens used in the current tests were typically biotinylated ovalbumin (a simulant) and cholera toxin; however, human immunoglobulin G (IgG) models were frequently employed in initial studies. Streptavidin (SA)-horseradish peroxidase (HRP) conjugate is used for the enzyme-linked assay.

The proposal described the use of thiol/carboxyl difunctionals to introduce carboxylic functionals to a gold surface. Initial experiments employed mercaptopropionic acid (MPA) and mercapto succinic acid (MSA). These short thioalkanes performed poorly, although mercaptoethanol exhibits strong reactivity to the thiol residues of a PMS coating. Based on this and similar studies, PMS and other silanes were considered in the Phase II tests.

ng/mm² ALP bound for various treatments

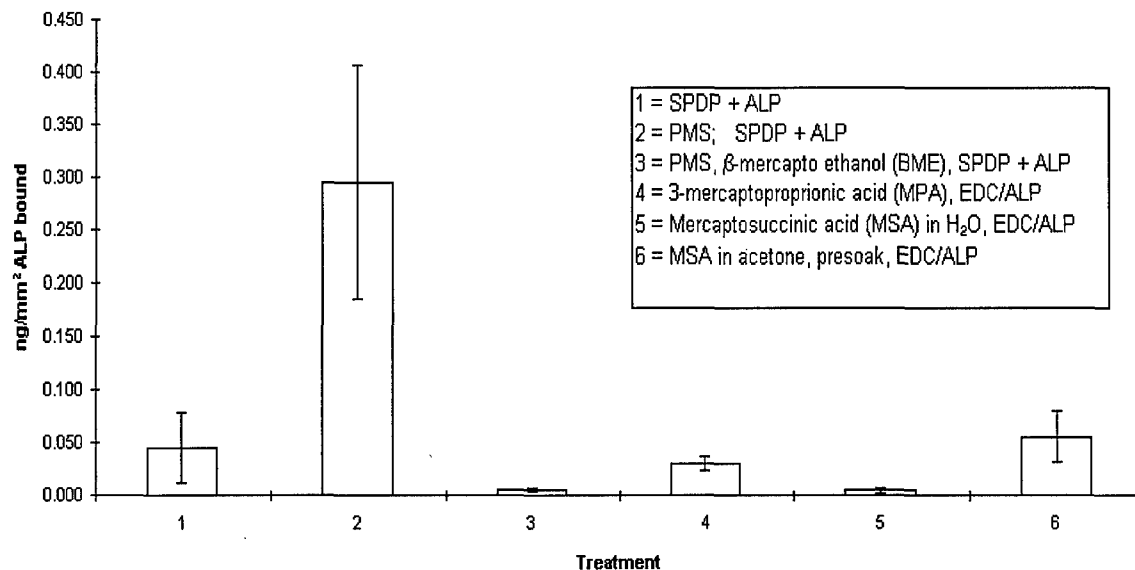


Figure 1. Comparison of the binding capacity for several strategies involving thiols on gold surfaces. Poly-mercaptopropyl methylsiloxane (PMS) provided good coupling of thiol-modified proteins to gold surfaces.

Silanes were found that are commonly used as adhesion promoters to gold and coat the surface with active silanol (e.g. reactive SiO-X) groups. These could be used for direct attachment to pendant amino groups of proteins or may be condensed to form a surface of hydroxyl groups - ideal for subsequent treatment with an amino-silane. Two such compounds were examined, bis [3-(triethoxy silyl) propyl] tetrasulfide (BTS) and 2-(diphenylphosphino) ethyl triethoxy-silane (PS). The results of one study are given in Figure 2. The different treatments showed relatively invariant binding capacities.

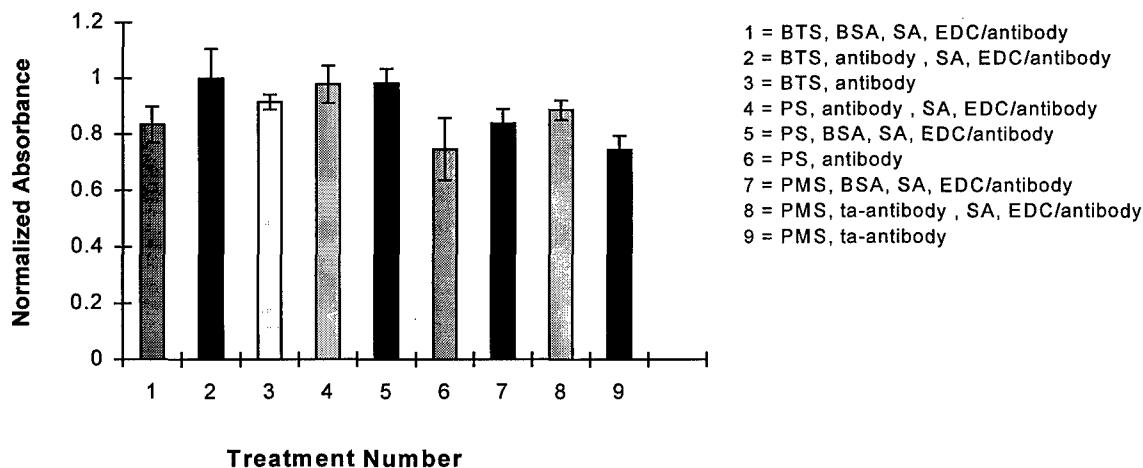


Figure 2. Attempts were made to take advantage of the silanol groups of BTS and PS. Succinic anhydride (SA) was used to carboxylate the surface for treatment numbers 1, 2, 4, 5, 7, and 8. All results are within their standard deviation of the overall average binding.

Figure 3 shows the results of an experiment comparing the binding efficiency of various treatments based on BTS to that of bare gold and the PMS / SPDP-antibody treatment. The study shows that treatment of Au with BTS, then aminopropyl triethoxysilane (APTES) is effective in aminating the surface, allowing for subsequent coupling of antibody via EDC (6). Still, PMS (1) exhibited better than 75% of the binding from (6). Meanwhile, carboxymethylcellulose (CMC), which should have dramatically increased binding, decreased it instead.

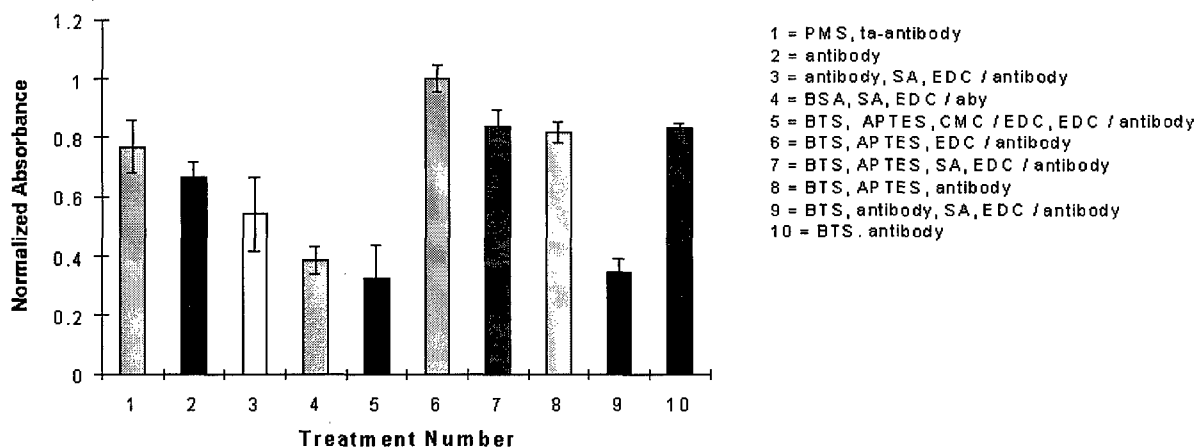


Figure 3. Of the various techniques, EDC / antibody introduced to a silanated Au surface shows the highest level of binding. The Au was silanated by first treating it with BTS and then APTES, leaving a coating of primary amines for subsequent coupling.

From previous experiments, high levels of antibody binding were observed for the BTS (Bis[3-triethoxysilyl]propyl]-tetrasulfide), APTES (amino propyl triethoxy silane) treated Au, with subsequent antibody attachment via EDC. It was desired to examine non-specific activity of various antigens to this surface as compared to the PMS treated Au, with attachment via thioalkylated antibody. This was done by introducing biotinylated cholera toxin to one chip set and biotinylated ovalbumin to another for each attachment procedure.

The self assembled monolayer (SAM) formed on gold by incubating gold chips in a 1% (wt/vol.) 11-mercapto-undecanoic acid (11-MUA) solution was also examined. The SAM forms a tough monolayer leaving exposed carboxyl groups for subsequent attachment to other molecules. This was also included in the study mentioned above. The results are shown below in Figure 4.

The PMS, thioalkylated antibody and 11-MUA, EDC/antibody procedures were about the same within one standard deviation. Both showed significant signal to noise ratios. The BTS/APTES procedure showed high levels of binding but also had high levels of non-specific activity towards ovalbumin. The BTS/APTES film wets in a low pH solution compared to a high pH solution as expected for an ammoniated surface. This could be observed by the naked eye. The carboxylated surface of the SAM showed the opposite effect, as expected. Therefore, despite previous data indicating that BTS/APTES provided high binding density, the technique appears to be uncontrolled and provides poor selectivity.

Non-specific binding for different aby attachment procedures

Antibody attached: anti-choleraenoid

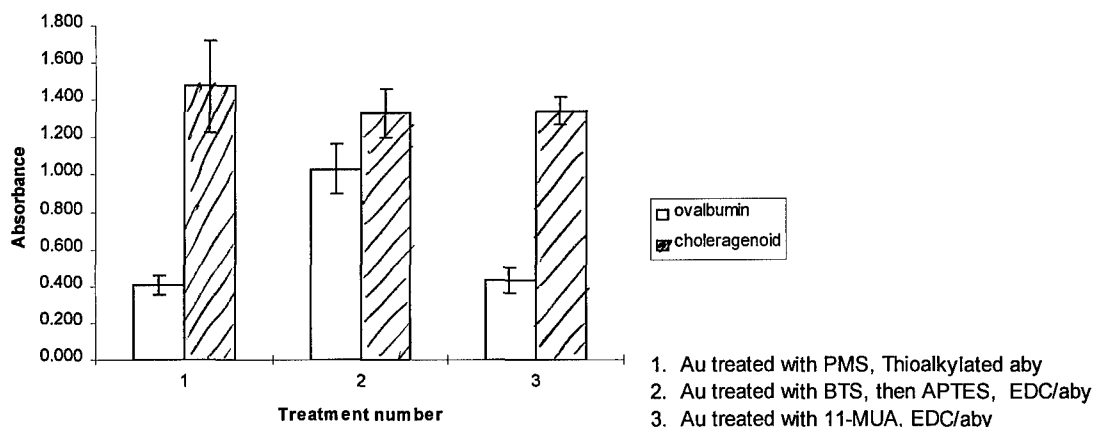


Figure 4. Au chips treated (2) with BTS/APTES show a high affinity for non-specific antigen. Treatments using PMS (1) and MUA (3) are comparable and exhibit reduced nonspecific binding.

Since proteins have a high affinity to gold, by either charge-charge or hydrophobic interactions, attempts were made to enhance these interactions. This included treating the gold surface with a long-chain thioalkane (octadecyl mercaptan) and exposing the resulting hydrophobic chips to an antibody solution. The resulting binding density was compared to that of gold treated with short chain, hydrophilic mercaptans (mercapto-propionic acid) and with bare gold. The pH of the antibody solutions was varied as well. Results indicate that only slight binding differences exist between octadecyl mercaptan treated chips compared to the PMS procedure or other hydrophilic treatments. Since attachment wasn't significantly increased, this approach was not pursued further. Variations in pH seemed to have the greatest effect on non-covalent binding to bare gold. The binding to bare gold was enhanced at low pH but the binding to treated surfaces was minimally affected. This could be due to amine-gold interactions between the protein residues and the gold surface. ***These results imply that covalent binding has superior stability over environmental and chemical conditions, as maintained in our proposal. Based on FY1 studies, both PMS (with thioalkylated antibody) and MUA (with EDC condensation to untreated antibody) provide acceptable binding properties. Chemical tests and biochemical longevity tests are described which further compare these techniques with cross-linked thiodialkyne analogs of MUA films.***

II.A.3) Regeneration and Storage

Regeneration studies using polyclonal antibody to B-choleraenoid and biotin labeled choleraenoid were employed to evaluate several potential regeneration buffers. Streptavidin-HRP was employed as the reporter in enzymatic assays. Seven solutions were compared, namely: (1) glycine-HCl (pH 2.5) and saturated urea (80%), (2) 50% glycine-HCl (pH 2.5)/saturated urea plus 50% ethylene glycol, (3) glycine-HCl (pH 2.5) in ethylene glycol (80%), (4) 4M guanidine HCl, (5) 50% urea / 50% ethylene glycol, (6) glycine HCl (pH 2.5), and (7) 0.1M Tris buffer + 50% ethylene glycol (pH 10). An eighth set employed no regeneration and serves as a reference for bound choleraenoid. Figure 5 shows the data on residual antigen for each chip set.

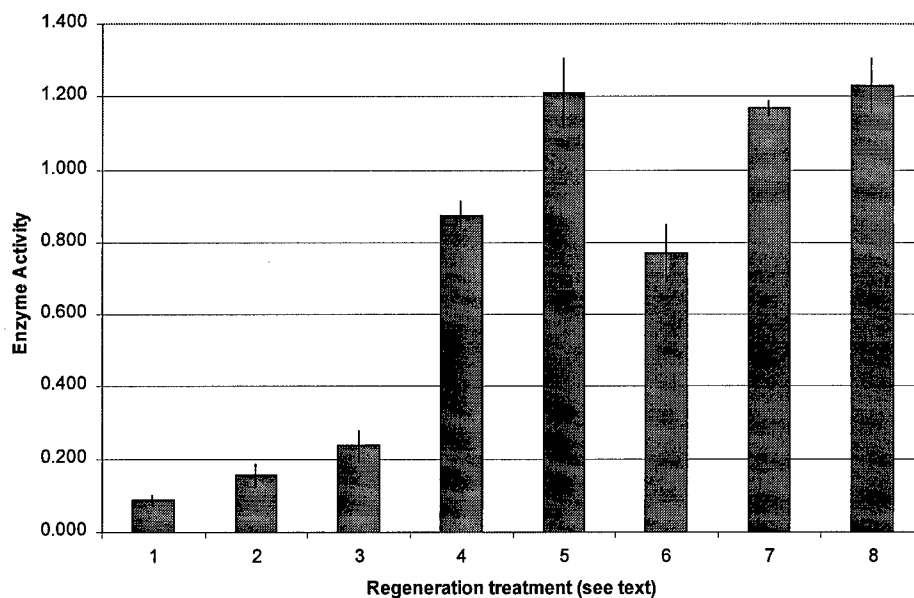


Figure 5. Residual antigen after the regeneration treatments discussed in the text.

Activity of the regenerated antibody in chip sets 1-3 were evaluated and compared to a fresh chip set in Figure 6. All three techniques exhibited comparable survivability; however, technique 2 exhibited slightly better survivability at the expense of slightly worse regenerative efficiency. This technique, employing urea, ethylene glycol and glycine-HCl was selected.

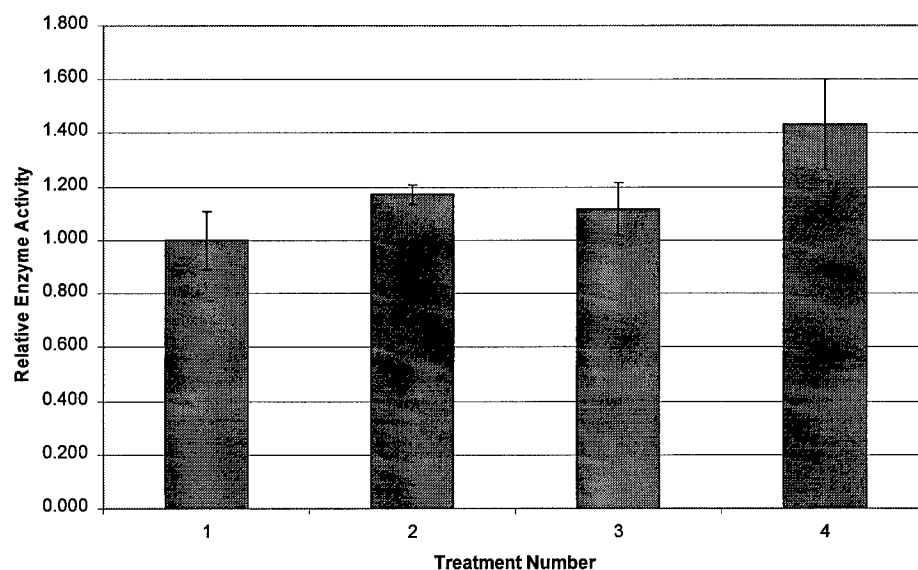


Figure 6. Enzyme activity as a measure of bound antigen after regeneration for treatments 1-3 in comparison to a fresh chip set.

Figure 7 presents the results of repetitive regeneration and reuse assays on six chip sets. Each chip set had been regenerated and reused the indicated number of times, with the fresh chip never having been regenerated. Since each data point corresponds to a unique chip set, a 20% range is reasonable and may be attributed to slight variations in surface area or the initial binding capacities, as well as in the regeneration and reuse process itself.

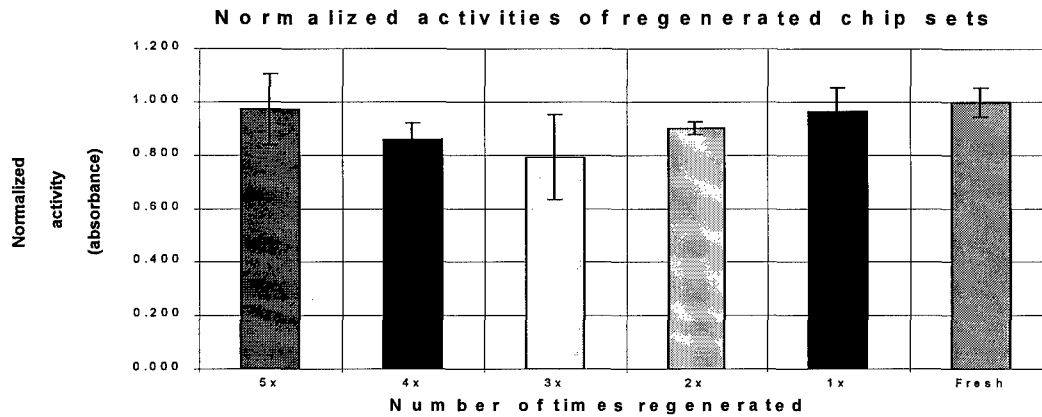


Figure 7. Regeneration using glycine-HCl, ethylene glycol and urea mixture provides no significant deterioration of the PMS-mediated antibody attachment. The activity dip for 3X regeneration and increase for 5x regeneration are associated with large standard deviations. A 20% variation between groups of chips is consistent with variations in surface area.

Longevity studies of anti-cholera attached to gold via SPDP have been ongoing. Short term data is presented in Figure 8. Five months of data are presented in Figure 9. Prior to this study, a batch of chips was coated with antibody and stored either in phosphate buffered saline with azide (PBA) and refrigerated, or treated with postcoat, dried and stored in an air tight container. Postcoat is comprised of sugar and proteins which help stabilize and protect antibodies when dried onto a solid. Each month, a fresh chip set was coated to serve as a reference. A fraction of the aged chips are withdrawn and tested. Immunochemical activity is evaluated for each chip set and fresh chip activity is employed as a normalization factor.

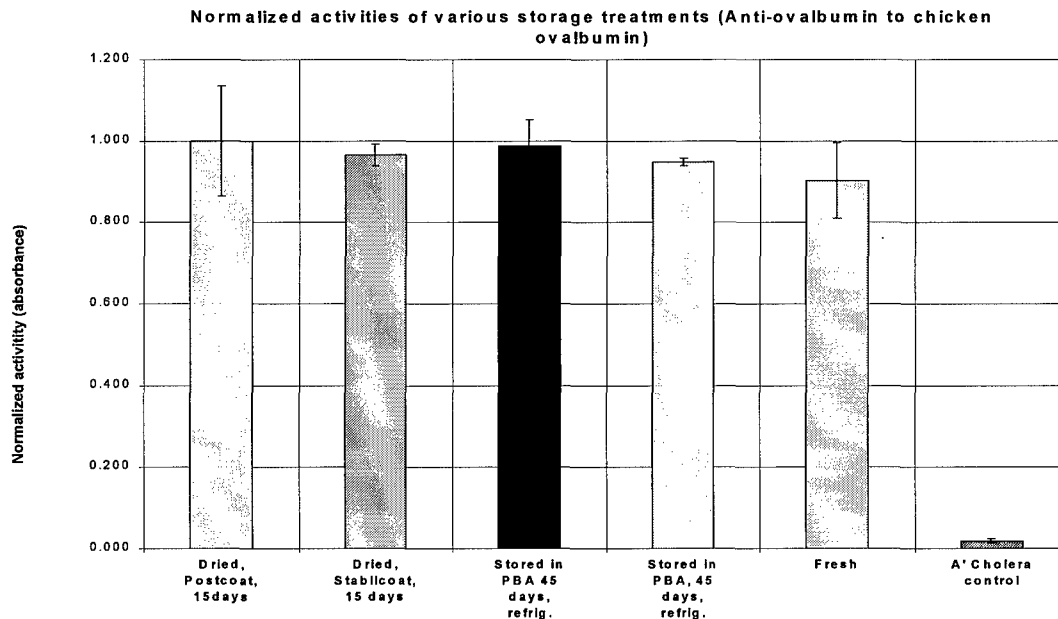


Figure 8. 15 and 45 day stability of anti-ovalbumin coated gold chips compared to fresh chips. Selectivity is demonstrated using a control set coated with anti-cholera antibody. No significant difference is observed. Postcoat was chosen for further study.

Normalized activities of A'Cholera vs Time

Attached via SPDP to PMS treated Au
Normalized to the activity of freshly prepared chips

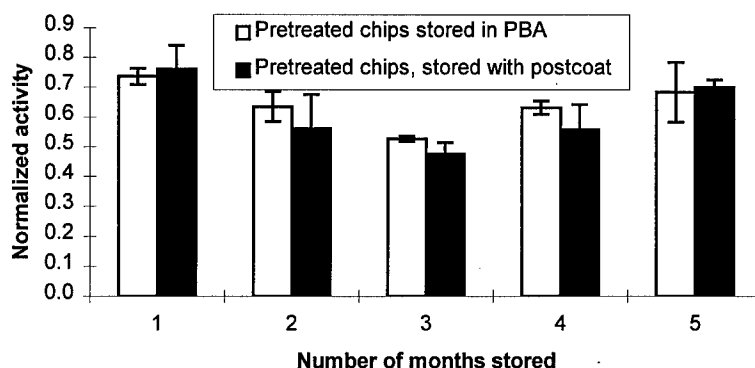


Figure 9. Attachment of anti-cholera thioalkylated antibody to Au via the PMS procedure seems to maintain its activity for at least 5 months. Dips in the activities are due to process variations.

Figure 9 shows that activities of the postcoat treated chips are comparable to the ones stored refrigerated in PBA. It appears that some activity is lost due to storage (25% to 50% activity loss); however, it is equally probable that the "fresh" chips were coincidentally at the high end of the distribution for antibody binding density.

II.A.4) Strip and Reuse

Electrochemical techniques (described below) appear to be ideal for the wholesale removal of antibody films, resulting in a bare gold surface. Further refinement of this renewal method will be pursued in FY2.

II.A.5) Antibody Selectivity (from DAAM01-95C-0076)

Results with this approach have been reproducible and offer good selectivity and sensitivity, as seen in Figure 10.

II.A.6) Radiolabeled Antibody Studies

Enzyme studies of binding density have been under question and an absolute measure of binding was desired. Radiolabeled antibodies were employed and were compared to frequency and enzyme measurements. Four quartz crystal microbalances (QCMs) were ultraviolet (UV) cleaned and then baseline air measurements were taken for each crystal using an impedance analyzer to determine the center frequency. They were then placed in an MUA solution for over 24 hours and subsequent measurements were taken to see if the monolayer had actually formed on the gold surface. The next step was to attach the radiolabeled antibodies to the surface using EDC condensation. The antibodies were exposed to the gold electrode for one hour and then subsequent impedance measurements were taken. Bovine serum albumin (BSA) was allowed to coat each chip for 30 minutes before measurements were taken using the analyzer. The devices were then exposed to a mock antigen (goat IgG) which should not bind because it is not specific to the antibody on the gold surface. After 30 minutes of exposure, measurements were taken using the analyzer. The final step was to expose three of the devices to the specific antigen (Human IgG-alkaline phosphatase conjugate), and one

device to a mock antigen (a non-immune goat IgG). The theory behind this was to use one of the devices as a control. After 30 minutes of exposure, measurements were taken using the analyzer. After all of the electronic measurements were taken, two other experiments were performed. One was a radiation test to find out if there actually were antibodies on the gold electrode surface. The other was an enzymatic assay, which would show if there were any antigen bound to the surface and the concentration of that antigen.

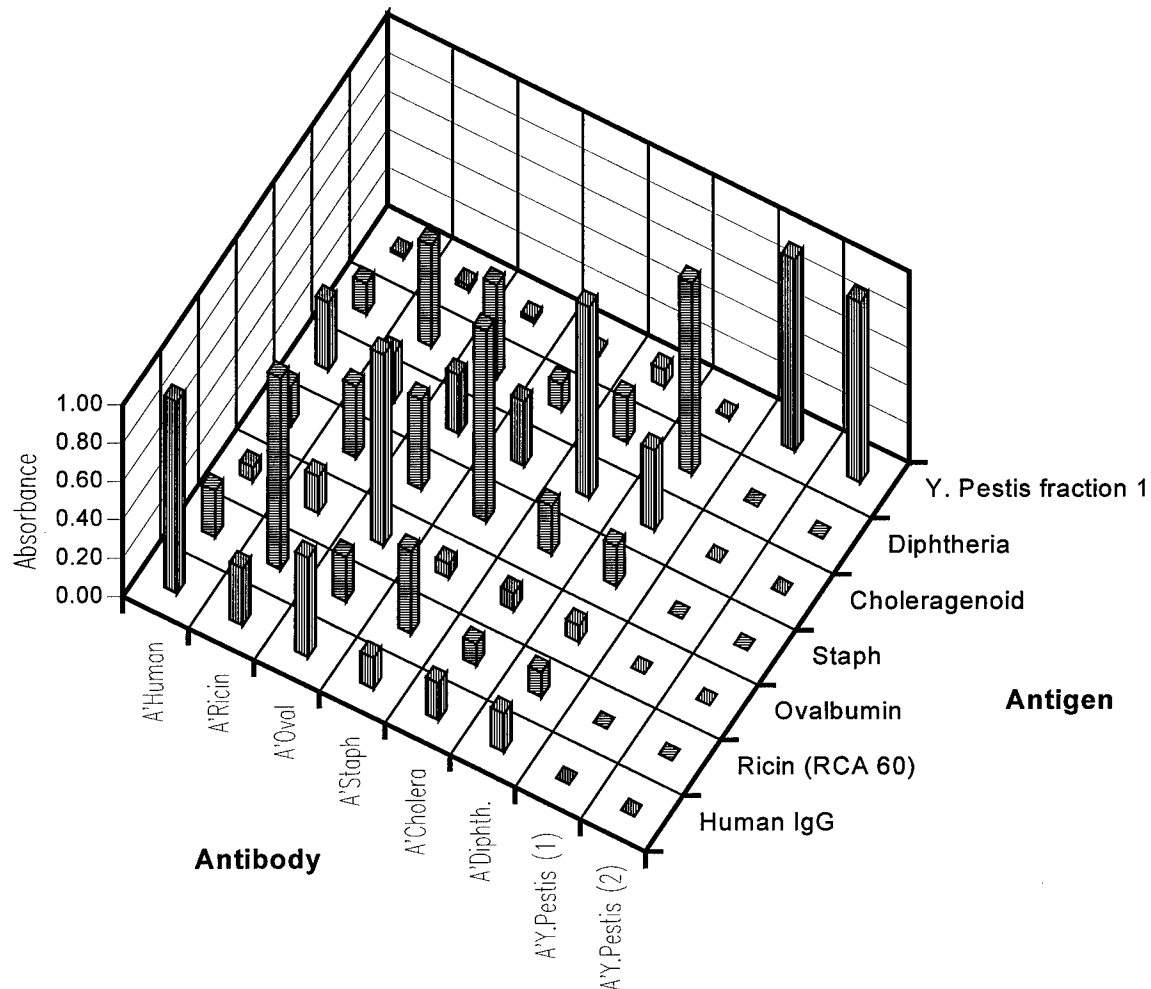


Figure 10. ELISA studies were employed to evaluate cross-reactivity matrix for eight antibodies to seven antigens. Each ELISA assay is normalized by row (Antigen). Further studies will verify some potential cross-reactivities.

Frequency shifts were inconsistent and are not shown here. Radioactivity indicates that the binding densities for the four QCM devices were 0.88, 0.85, 1.2 and 0.86 ng/mm², respectively. These binding densities are consistent with most ELISA tests, literature data and theoretical binding capacity. The packed monolayer density for IgG on an ideal surface is approximately 10 ng/mm². At this point, the antibody would be inactivated to steric hindrances. Enzyme studies indicated low binding efficiencies (as low as 2 to 4% for IgG capture by anti-IgG). Antibody activity has been found questionable, preventing any conclusive determination of the accuracy of solid-phase HRP studies. Further experiments will be pursued to quantitate binding.

II.A.7) Thiol-Gold Surface Chemistry

II.A.7.a) Preliminary Effort and Implications

A secondary task relative to antibody immobilization has been the development of methods to characterize the coverage of PMS and self-assembled monolayers (SAMs). In particular, SAM surfaces based on hexadecanethiol (HDT) and eicosa 5,7-diyne thiol (a thiodialkyne acid) were characterized using available equipment and macroscopic techniques in order to find a way to evaluate monolayer coverage on gold chips. This is important to the research since inconsistent treatment in the first step is not detectable until the enzyme step using biochemical techniques. In the long term, this is important as a quality control technique.

X-ray photoelectron spectroscopy (XPS) investigation of HDT on gold surfaces resulted in good spectra including a small but definite peak for sulfur. The predicted carbon peak is also present, but because carbon can sometimes advantageously adhere to surfaces, the existence of the sulfur peak corroborates the existence of the HDT monolayer. Other experiments are planned, including angle-dependent analysis, which can give some information about the monolayer such as identity of groups in the chain. XPS of chips with antibody attached show a strong nitrogen peak, as expected. XPS has proven valuable in research phases but is too expensive to be employed as a quality control method.

External Reflectance-Fourier transform infrared (ER-FTIR) spectra of three samples have been acquired: control gold chip, HDT monolayer, and the eicosa-diyne monolayer. Problems with the equipment have inhibited getting hard copies of the ratio spectra, but the data appears to be reproducible and peaks are in the appropriate areas. However, the peaks are rather broad. Most notably, there is a difference in the spectra near 2160 cm^{-1} , as expected due to the presence of triple bonds. More work has to be done to convert the data into the $-\log(R/R_0)$ format, as reported in the literature and to obtain quantitative data.

Atomic Force Microscopy (AFM) measurements have been performed. Several scans of the monolayer surface have been performed to evaluate the ability of this method to detect defects in the monolayer surface. Scans show unevenness in the surface, however, it is not clear if this is caused by unevenness on the initial gold surface or in the monolayer coverage.

Etch techniques were evaluated to determine if the film would deter gold etch. KI/I_2^- etches both the control and monolayer-coated chips rapidly, and thus, cannot be used to distinguish between them. An etchant based on $0.1\text{M KCN} / 1\text{M KOH}$ is more promising. When O_2 is bubbled through the KCN / KOH and a drop placed on a gold chip, etching can be seen on the control (gold) chip 15 min after a drop has been placed on the chip. The two different monolayer chips (HDT and eicosa) exhibit less etching in the same time frame although some is visible to the naked eye and under the microscope. Experiments are being done to verify the necessary drop size and optimum time needed to differentiate between the chips. The eicosa monolayer chip was photolyzed for five minutes in a nitrogen atmosphere, which should cause polymerization of the diyne groups of the chain. This should make the monolayer more robust. In treatment with the KCN / KOH etch (one drop on the surface for eight minutes) a slight etching was observed that was similar to the HDT and the unpolymerised eicosa monolayer chips. Finally, an etchant based on $\text{K}_2\text{S}_2\text{O}_4 / \text{KOH} / \text{K}_3\text{Fe}(\text{CN})_6 / \text{K}_4\text{Fe}(\text{CN})_6$ is (according to the literature) supposed to be the fastest, most discriminating gold etch; however, it failed to etch either the control (gold) or monolayer-coated chips. More research is being done to get results with this etch because it is the most benign mixture, both environmentally and to humans. Nonetheless, it appears that etch techniques are generally destructive; however, single scan electrochemistry is not.

So far, electrochemistry seems to be the most reproducible way to detect the presence of the SAM on a gold surface. A series of experiments have been done using $\text{K}_3\text{Fe}(\text{CN})_6$ as the redox species. When a plain gold surface is measured, an easily discernible waveform is

detected at a scan rate of 100 mV/minute and a window of -1 to +1 volts. SAM-coated surfaces do not exhibit this waveform. The cyclic voltammogram is a relatively flat line. The setup uses a system where it is easy to replace the gold chip and therefore test chips relatively quickly. In a processing environment, this would be a simple test to verify SAM functionality. The chip is put on a ceramic plate with the Ag/AgCl reference electrode secured in a perpendicular position. The counter electrode, a Pt wire, is attached to the right of the chip and bent so that it is over the surface of the gold chip, but not touching. The working electrode is a gold wire that is in contact with the gold chip. A drop of 10 mM $K_3Fe(CN)_6$ solution is placed with a pipette between the reference electrode and the gold surface enclosing also the counter electrode. This takes about three drops from the pipette for a substantial drop. The CV can then be performed. The chip can be slid in and out for rapid testing. Scanning variations could be applied to arrays of sensors on 3" wafers, as would be required in production.

It appears that partial monolayers can be detected because some variation of the $Fe(CN)_6^{-3}$ waveform is detectable with monolayers that have been in various etches or where the chip has purposely been made so one half is monolayer and one half is uncoated gold surface. Repeated scans (20) between +1V and -1V wrt Ag/AgCl cause desorption of MUA, HDT and non-cross-linked thiodialkynes, shown by the development of the reversible $Fe(CN)_6^{-3}$ peaks. This implies that the SAM is electrochemically removed during the process. This could be applied to the wholesale removal of biorecognition layers in order to "reprogram" a sensor.

II.A.7.b) Further Electrochemical Studies

The stability of crosslinked dialkyne ($C\equiv C\equiv C$) self-assembled monolayers has been examined and compared to that of unsaturated long chain thiols (HDT-hexadecylmercaptan and MUA-mercaptoundecanoic acid). The resulting COOH surfaces have been characterized using XPS, electrochemistry and measurement of the attachment of IgG to the acid surface.

Reference compounds

T1 - HDT hexadecylmercaptan

T2 - MUA mercaptoundecanoic acid

D1 - 5,7,-eicosa diyne-1-thiol

D2 - $CH_3COSCH_2C\equiv C\equiv C(CH_2)_8COOCH_3$ - protected diyne thiol

D3 - $HSCH_2C\equiv C\equiv C(CH_2)_8COOH$ - deprotected thiol

FS#1 - chip soaked in protected thiol (analogous to D2) [chips sent by Frank Smith]

FS#2 - chip treated with NH_3 to produce 14-mercaptomethyl ester[chips sent by FS]

FS#3 - chip soaked in deprotected thiol (D3) [chips sent by Frank Smith]

Table 1. Compounds studied using electrochemical and XPS methods.

Thiodialkyne sample, D2, was deprotected to yield sample, D3, by the method outlined by Frank Smith [6] and was compared to protected thiol sample, D2, to determine if thiol monolayer would form even with the CH_3CO protection group attached to the sulfur. XPS data shows acetyl protected thiol still forms a layer, but with less coverage than the deprotected thiol, based on the intensities of the C1s and O1s peaks.

XPS analysis indicated that monolayers are formed consistent with the starting material. In the S(2p) spectra, however, a peak appears in several of the spectra at 167 eV binding energy. The thiol peak is consistent at a binding energy of 163 eV. The presence of this additional peak might indicate a more oxidized sulfur species, which is also on the surface. This is possible with the protected thiol sample but is not consistent with a tightly packed homogeneous monolayer formation. Further investigation and verification of this peak are planned. Separate samples sent by Frank Smith were analyzed and compared with samples prepared here. Results were comparable.

Cyclic voltammetry (CV) studies indicate that the monolayers made with the thiodialkyne, D1, which have been photolyzed under nitrogen, maintain their integrity after 32 CV cycles from +.6V to -.6V. Thioalkane, T1, monolayers show a gradual increase of the redox wave of the $\text{Fe}(\text{CN})_6^{-3}$ after 2 CV cycles with the same limits, indicating desorption of the thioalkane and exposure of the underlying gold.

Electrochemical investigation of thiodialkyne, D3, in 1M KCl indicates that the gold surface becomes oxidized between +1.0V and +1.2V, leaving a totally etched circle on the chip. Control (uncoated) gold chips oxidized at +1 V. The thiodialkyne, D3, monolayer shows no reversible wave for $\text{Fe}(\text{CN})_6^{-3}$ when tested for ranges 0 to -.7 (-1.0, -1.2, -1.5), however at -1.5 gold reduced leaving an etched surface. It appears that the cross-linked (photopolymerized) diyne SAM adheres at least as well as the gold itself. Crosslinked thiodialkyne monolayers appear to be stable over the electrochemical range -1.2V to +1.0V over repeated potential cycles.

Comparison of CV scans in electrolyte (NaClO_4) and with $\text{Fe}(\text{CN})_6^{-3}$ show differences in current intensity between surfaces with attached antibody and those without antibody attachment. Comparison of control chips (cleaned plain gold surface) show differences in current intensity also and a shifting of the redox peaks of the $\text{Fe}(\text{CN})_6^{-3}$ when exposed to the antibody indicating some antibody sticks to the gold surface but not enough to prevent redox events. Electrochemical screening appears to be a viable tool for quality control for antibody attachment. Electrochemical indications that antibody sticks to bare gold is consistent with biochemical studies.

These experiments confirm literature results that indicate that a cross-linked thiol has considerably better stability than simple monolayers. It further indicates that electrochemical techniques can be employed as quality control steps in the manufacture of biosensors. Finally, the ability to perform electrochemical evaluations through attached antibody films offers both a quality control technique and a potential method of regenerating the sensor (i.e. releasing toxin) without acid wash.

II.B) Piezoelectric Sensors

II.B.1) Scope and Schedule. Extensions to Scope.

Lithium tantalate shear horizontal acoustic plate mode (SHAPM) properties were theoretically studied in order to compare the resulting SHAPM properties to the results of a similar quartz search, separately funded. This task has been completed. Materials' screening has been completed. Initial designs have been performed and additional designs are being prepared.

Surface transverse wave (STW) effort has been delayed from the projected schedule due to difficulties in depositing suitable polycrystalline dielectric coatings. This is a critical limitation; however, BIODE intends to continue efforts in this area, due to the extreme improvement in sensitivity offered by STW devices (as much as 100-fold, measured). An upper limit on frequency appears to exist between 500 and 1200 MHz. The limit is due to viscous losses. The same mechanical behavior that determines mass sensitivity also determines viscous losses in the solution. The limit corresponds to mass sensitivity substantially exceeding 10 pg/mm^2 bound mass at 1 parts per million (ppm) frequency resolution ($100 \text{ ppm-mm}^2/\text{ng}$).

Monolithic piezoelectric sensor (MPS) efforts that extend quartz crystal microbalance (QCM) technology are encouraging. BIODE and the University of Maine have filed a joint patent relating to the MPS structure. Initial results relating to fluid phase operation are encouraging. The MPS appears to offer similar sensitivity to the best SHAPMs at frequencies as low as 3.3 MHz and would exceed the sensitivity of an STW, if it were possible to operate at the same frequency.

II.B.2) Overview of Shear Wave Piezoelectric Sensor Geometries

Piezoelectric shear-wave technology exhibits the desired direct detection of target biochemical toxins in simple response and recovery measurement cycles. *Based on direct comparisons reported in the literature [7] the least effective piezoelectric sensor implementations are at least as sensitive as current state of the art surface plasmon resonance (SPR) systems. Sensor / reference pairs have substantially reduced undesired volume effects, thermal effects and nonspecific effects. Arrays of multiple sensors have been demonstrated with piezoelectric technology.* Based on the issues of integration, selectivity and field portability, piezoelectric sensors are the most attractive. Thus, the proposed work will employ shear wave piezoelectric sensor technology.

There has been a great deal of development of piezoelectric sensors for chemical and biochemical detection. While there have been substantial successes in gas sensing, fluid phase detection solutions have proven difficult to implement. Nonetheless, a number of highly sensitive ($< \text{ng} / \text{ml}$) piezoelectric biosensors have been demonstrated in the literature [1]. Table 2, below, outlines the relevant sensor geometries along with the most pertinent properties.

Feature of the Sensor	QCM	SHAPM	STW	MPS
Single mode Response	yes	somewhat	yes	yes
3 terminal device	no	yes	yes	yes
Temperature stability	excellent	good	good	excellent
Mass sensitivity	nanogram	< nanogram	picograms	<nanogram
Compressional modes	problem	good	excellent	design issue
Oscillator stability	several ppm	<1 ppm	<1 ppm	<1 ppm?
Separate electronics and sensing surfaces	no	complete	thick film	complete
Potential sensor array dimensionality	2	1	1	2
Manufacturability	excellent	good	complex	excellent

Table 2. Comparison of the salient properties of quartz crystal microbalance (QCM) shear horizontal acoustic plate mode (SHAPM) surface transverse wave (STW) and novel monolithic piezoelectric sensor (MPS). STW sensors exhibit the best performance at the expense of manufacturability. The proposed MPS offers excellent overall properties.

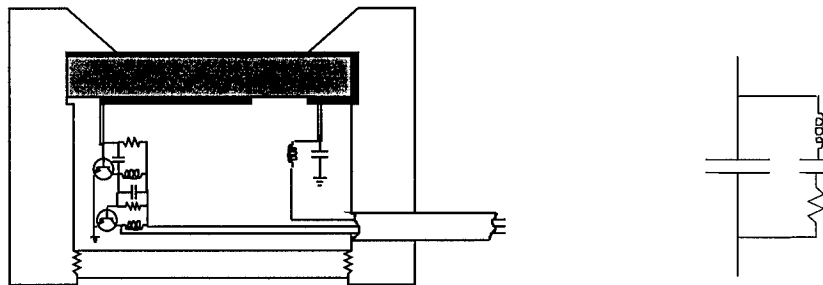


Figure 11. The traditional quartz crystal microbalance (QCM) sensor consists of a piezoelectric crystal with metal electrodes on both surfaces. The region between the electrodes supports a mechanical standing wave. Electrical connections are made to the grounded side through the case and to the positive side via a wire point contact. Typically, the oscillator electronics are placed in the sensor package. The QCM electrical model consists of a parallel capacitance and a series resonant circuit.

Of the available piezoelectric sensors, the best known candidate is the simplest and oldest structure, namely the QCM, which is shown in Figure 11. The QCM obtained its reputation based on the stable oscillator properties of air-loaded and vacuum-loaded quartz crystal

oscillators. These oscillators provide extremely stable frequency sources with respectable sensitivity to mass and interfacial perturbations. The extremely high stability is a product of three separate properties of the sensor. First, the shear wave employed in AT-cut quartz resonators exhibits outstanding temperature stability for the air-loaded series resonant frequency of the QCM. Second, the air-loaded quartz resonator exhibits a well-defined, high quality (Q, defined as energy stored / energy lost) resonance. A benefit of high Q is a narrow spectral linewidth and a steep slope of phase with respect to frequency, such that small external changes in electrical phase lead to small frequency errors. Finally, the oscillators typically employed a Pierce-type structure such that the series resonant crystal provided most of the total phase shift and was thus the overwhelming factor in determining the exact oscillation frequency.

The positive properties of air-loaded QCMs minimized many second order performance factors that now plague frequency based measurements of fluid-loaded QCMs. The Q factor of a fluid loaded QCM is very low compared to its air-loaded counterpart. This has serious impact on the stability of the oscillator over random changes in the phase of external circuit elements. More important is the fact that the oscillation frequency may be well removed from the series resonant frequency. The correlation between mechanical perturbations and measured frequency is then poor since oscillator frequency is a complicated function of the series resonant frequency, parallel resonant frequency, the Q and external parasitic influences [8,9,10].

Commercially available electrochemical plating QCM sensors and oscillators have been measured. The oscillators exhibited 1 Hz stability at a nominal frequency of 5 MHz when operated in air. When small fluid volumes were placed in a fluid cell on the sensor surface, as required for DNA detection, extremely poor stability was observed. The use of a reference oscillator did not compensate the QCM, indicating that the oscillator frequency variations were not systematic. Finite fluid geometry may have been problematic since fluctuations in the fluid boundaries may have affected the interaction between the QCM resonance and the fluid [11,12]. A QCM viscometer was borrowed from Sandia National Labs, which exhibited excellent stability when immersed (better than ± 2 Hz) but was also not stable with a small, finite fluid load. While these properties were suitable to large deposition baths and fluid samples, biochemical detection typically involves small samples. Early results indicate that the QCM has serious drawbacks when applied to low-volume biochemical detection.

Researchers have overcome some of these problems by employing spectroscopic techniques [13,14,15]. In these methods, crystal impedance is measured as a function of frequency and curve fit to well-known models to extract film properties. These techniques simultaneously offer information about multiple properties of the QCM. While these techniques are very effective, the equipment is substantially larger and more expensive than the alternative oscillator electronics. In addition, substantial computational effort is required to curve fit the spectroscopic data. Oscillators are still generally preferred [8,16,17] by well-respected researchers. Because of the performance limitations related to fluid-loaded QCM oscillators, BIODÉ proposes to employ alternate piezoelectric sensor implementations, which offer suitable oscillator performance. These implementations are favored since the current application demands the simplicity and power efficiency associated with oscillator-based electronics.

Both Sandia National Labs [18] and BIODÉ [19-23] have studied the SHAPM sensor geometry, which is shown in Figure 12. Martin et al. have focused on high symmetry orientations, such as ST quartz, in order to obtain simple acoustic modes with integral numbers of half wavelengths of transverse variation. These orientations behave in an intuitively acceptable manner; however, it is difficult to design electronics which oscillate on a single acoustic mode. BIODÉ has chosen to employ SHAPMs that are derived from "leaky" surface waves. These modes provide enhanced mechanical displacements at the crystal surface and exhibit a single acoustic mode with enhanced electrical efficiency up to a limiting frequency-thickness product. The drawback of these modes has traditionally been the poor temperature sensitivity of the lithium niobate crystals. More recently, BIODÉ has identified quartz crystal

orientations that exhibit a single, predominately-shear, temperature stable acoustic mode with acceptable electrical efficiency [24,25], eliminating this drawback. Nonetheless, suitable biosensor devices have not been obtained due to the sensitivity – stability tradeoff. The applicability of the SHAPM is limited by the existence of other, potentially interfering, acoustic modes of the plate.

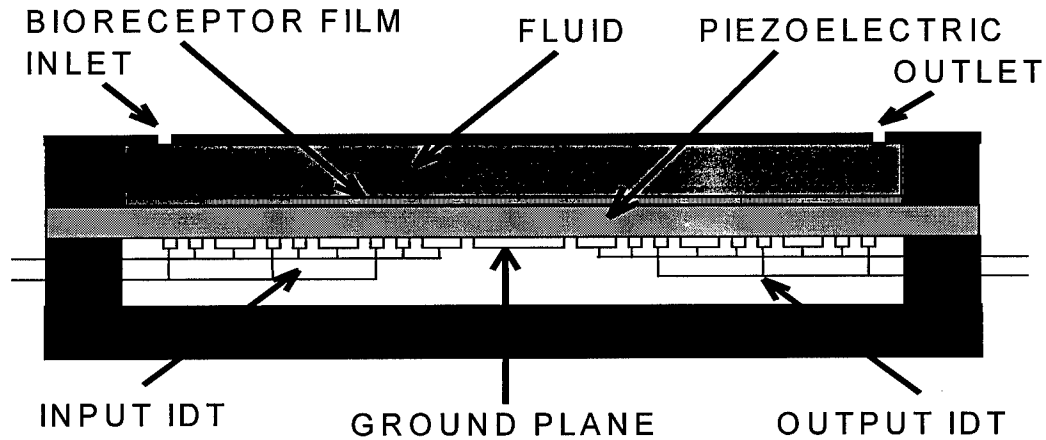


Figure 12. Cross-sectional view of the Shear Horizontal Acoustic Plate Mode (SHAPM) device, showing a piezoelectric plate (cross-hatched), input and output interdigital transducers (IDTs) separated by a ground plane, a bioreceptor film (vertical lines), fluid containment cell and an analytical fluid solution (diagonal lines). The fundamental advantage of the SHAPM is the separation of the electronics from the fluid.

Higher operating frequencies and simplified electronic design may be achieved using the STW sensor structure, which does not support potentially interfering spurious modes. In this sensor a single, temperature stable STW is excited without resorting to thin plates. The STW propagates perpendicular to the X-axis in rotated-Y cuts of quartz and has only shear-horizontal (SH) displacements. In uncoated crystals, the acoustic energy of these waves is largely internal to the crystal and surface perturbations are minor, resulting in low sensitivity and poor electrical efficiency.

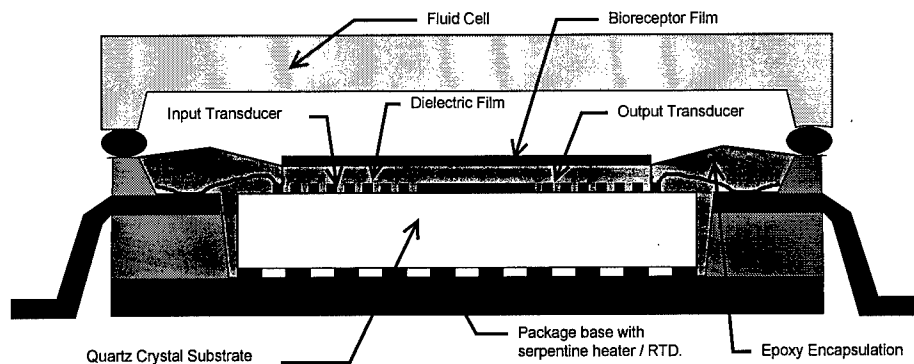


Figure 13. The proposed STW sensor employs the aluminum IDTs and a dielectric film overlay to trap the wave. The aluminum layer also implements the electrical function of the device while the dielectric layer eliminates capacitive loading of the transducers by the fluid. A serpentine resistive thermal device (RTD) is used to both measure and control temperature. The bioreceptor film typically includes a gold layer, suitable crosslinking chemicals and the genomic probe.

Josse first demonstrated that a sputtered dielectric layer (e.g. fused silica) would trap the acoustic wave to the surface, increasing the electrical efficiency [26]. Several researchers have demonstrated sensor prototypes of the STW (a.k.a. Love wave) sensor [27-31]. Figure 13

depicts the geometry of the STW sensor, including electronic packaging and fluid cell. Aluminum interdigital transducers (IDTs) are employed to generate and receive the acoustic wave within a delay line configuration. While a resonator configuration is electrically superior when operated in air, there are several issues related to the electrical connections and viscous losses of the fluid which favor the delay line geometry. The silica overlay is employed in order to insulate the device from the conductive and dielectric loading caused by the fluid [2], as well as to further trap the wave. Finally, a metallic (e.g. gold) film may be deposited as a ground plane. This film also serves in the attachment of the antigen. At frequencies approaching 500 MHz, the STW sensor is quite small (2.5 mm by 5.5 mm) and is theoretically capable of detecting less than 10 picograms of bound mass. Higher frequencies (and sensitivities) are possible; however, viscous losses become prohibitive.

Table 3 summarizes some mass-sensitivity data for several candidate shear wave sensors at different operating frequencies. *While the surface transverse wave (STW) sensor offers extremely high sensitivity, manufacturing issues have prevented its applicability.* Other than the STW device, one sees that technology based on the thickness shear mode (TSM)- such as the QCM - offers the best sensitivity. The TSM sensors offer excellent sensitivity if suitably thin plates are employed. A practical limit for rugged TSM devices is on the order of 50 MHz (33 μ thickness). At these frequencies, a thin membrane is chemically milled from a thicker supporting plate. *The fundamental issue with this technology is to overcome the poor performance of the current QCM implementation and support instrumentation.*

Technology	Operating Frequency (MHz)	Temp. Coef. of Frequency (ppm/°C)	Sensitivity (ppm-mm ² /ng)	Sensitivity to TCF ratio
TSM	3.3	±1	0.9	>0.9
Quartz SHAPM	193	±2	0.6*	>0.3
LTA SHAPM	62	-26	0.6*	0.023
LNB SHAPM	48	-76	1.1	0.014
TSM	50	±1	14	>14
TSM	500	±1	140	>140
STW	500	±2	120**	>60

Table 3. Mass sensitivity, defined as the fractional frequency shift in parts per million caused by a surface mass of 1 ng/mm², increases with increasing frequency. The proportionality and frequency dependence are determined by the specific material and geometry. Even at 5 MHz, the TSM exhibits sensitivity comparable to the most sensitive SHAPM devices. The indicated SHAPM frequencies represent the highest practical values for 0.5 mm thick plates, corresponding to a 3.3 MHz TSM. STW and high frequency TSM devices offer much higher sensitivity. (*directly measured. **extracted data.)

The ideal sensor would combine the material advantages of the QCM with the structural advantages of the SHAPM. BIODE and the University of Maine have recently invented a structure that eliminates the instrumentation problems of the QCM while retaining its favorable properties. The so-called monolithic piezoelectric sensor (MPS) employs monolithic coupled resonator filter technology to create a sensing element with the simplicity of the QCM but with separate electrical and sensing surfaces, as for the SHAPM. MPS technology offers good mass sensitivity with excellent temperature stability and inexpensive manufacture. The MPS sensor does share the issue of compressional mode generation with the related QCM; however, careful design can minimize these effects. Additionally, much more robust oscillator circuits are available because of the improved structure. The three-terminal configuration simplifies high frequency inverted mesa designs, which allow smaller lateral dimensions while still avoiding compressional waves.

II.B.3) Quartz SHAPM (from parallel project: DE-FG02-94ER-81717)

II.B.3.a) Pure SH Acoustic Plate Modes, AT-90 Quartz

Pure SH waves are relatively rare and occur under specific symmetry conditions of the crystal. For quartz, pure SH waves may be generated when the axis perpendicular to the plate and the axis of propagation both fall in the YZ plane of the crystal. These crystal cuts are commonly referred to as the 90° propagating rotated Y-cuts (RYC) and are employed in STW devices and bulk acoustic wave resonators. The APMs derived from these waves obey the theoretical model of Ricco and Martin [33], and there is typically no single dominant mode, nor is one mode more sensitive than another. A typical SHAPM spectrum for these waves is presented in Figure 14, which presents the data for AT-cut quartz propagating perpendicular to the X-axis. The assumed IDT period is 30μ and the plate thickness is 0.5 mm. This orientation is employed in the STW devices described previously and the relationship between the STW and these APMs will be discussed below. The key features are that the individual APMs have nearly identical and excessively low electrical efficiency and therefore it is difficult to design electronics which operate on a single acoustic mode. BIODE had attempted to design low frequency SHAPMs using these orientations several years ago with little success. Higher frequency devices may be more practical; however, as will be discussed below, the STW is a more promising use of these substrate orientations.

APM Electrical Efficiency vs Frequency

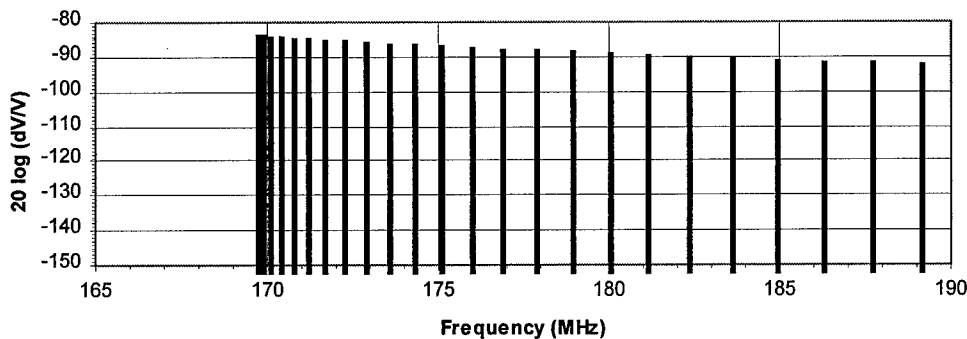


Figure 14. SHAPM spectrum for a pure SH orientation, such as AT-90 quartz (Euler angles 0, 126, 90). The electrical efficiency gradually tapers off and all modes have essentially the same sensitivity and coupling. Three modes were not resolved by the program, corresponding to the hyperbolic (evanescent) APM, the zero-order (constant amplitude) APM and the first order (asymmetric) APM, all of which would be virtually unresolvable from the mode doublet at 169 MHz.

A typical mode profile of such an acoustic wave is given in Figure 15, which corresponds to the lowest velocity mode at 169 MHz. The calculations were performed for the APMs in AT-cut quartz (which is also employed in STW devices). The mode has a mass sensitivity of -0.78 ppm- mm^2/ng at 169 MHz on a 0.5 mm thick plate. If the plate is thinned to 0.1 mm thick, the sensitivity increase is five-fold, in agreement with Martin's theory. As we will discuss below, these sensitivity values and the fact that the APM is temperature stable are promising. However, in order to resolve individual (higher-order) modes, the IDTs would require > 200 periods at a 0.5 mm thickness (>12 mm active device length).

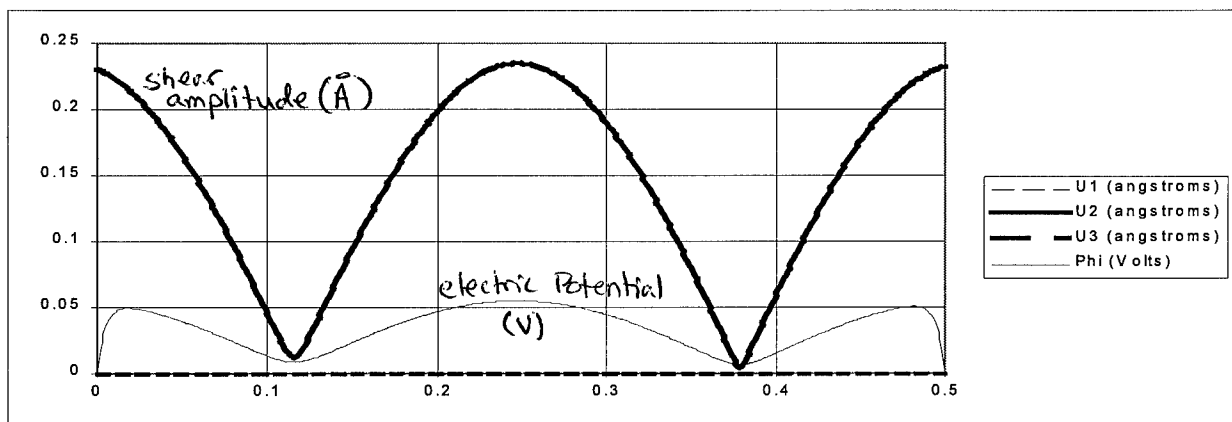


Figure 15. Mode profile for the pure-SH APM on AT-90 quartz. The acoustic wave velocity is $5.091 \text{ mm}/\mu\text{s}$, the attenuation is 0.000017 , k_2 is 0.00012 and the predicted mass sensitivity is $-0.78 \text{ ppm}\cdot\text{mm}^2/\text{ng}$. The X-axis represents depth from the fluid surface towards the IDT surface. The thick line is the magnitude of the shear horizontal (U_2) mechanical displacement in angstroms and the thin line is the electrical potential in volts. A conductor is assumed on both surfaces, causing the potential to be zero at each surface. The profile corresponds to a mode number of 2 (two half-periods of variation).

The major drawbacks to these pure SH orientations are three-fold. One is that the piezoelectric coupling is extremely low in standard (0.5 mm thick) plate thicknesses. Namely, k^2 is 0.00012 compared to 0.0012 for the Surface acoustic wave (SAW) on the well-known temperature compensated cut of quartz (ST-quartz) and 0.04 for the APM on ZX lithium niobate. However, as the plate thickness is decreased, the coupling improves and is 0.00058 at 0.1 mm ($1/2$ the value of the SAW on ST-quartz). The second problem is that it is extremely difficult to isolate a single acoustic mode. The coupling efficiencies are extremely uniform and the modes are closely spaced. Even using the relatively long transducers necessary to resolve a single mode, it would be impossible to employ an oscillator circuit without substantial external filtering. The third problem is that these APMs are potentially dominated by the STW which becomes strongly coupled if the transducer metal thickness becomes significant compared to the transducer period. For the 30μ IDT period evaluated above, the critical thickness is on the order of 5000 angstroms of aluminum and this might not be a significant problem. However, if the IDT period is reduced to 10μ in an effort to miniaturize the device and improve sensitivity, the structure becomes essentially identical to the existing STW design. In this case, the wave will become trapped to the IDT surface, and no fluid-phase sensing will occur. Since the trapped waves (STWs) have higher mass sensitivity than the APM at the same frequency, it appears reasonable to pursue STW devices over this class of APMs. In the event that BIODE fails to identify a suitable thick dielectric film for the STW (as discussed above), these APMs will deserve further consideration. In any case, devices designed for use as STWs may be polished to form SHAPM devices in order to verify the expected APM properties.

II.B.3.b) Description of Modes In Rotated Y-cut X-propagating APM Spectra

In order to provide context for the remaining discussions, a typical APM spectrum for rotated Y-cut quartz is given in Figure 16, which presents the coupling strengths, $20 \log(k^2/2)$, on the vertical axis and the APM mode center frequency on the horizontal axis. (The coupling factor, k^2 is approximately equal to twice the fractional velocity shift, $\Delta V/V$, caused by shorting the electric field). It should be mentioned that the computer program does not calculate the log for values below 10^{-5} (-100 on the chart) and modes with this amplitude may in fact have lower coupling. This should be considered the noise floor of the spectrum. The spectrum depicts the modes in a 0.5 mm thick ST-quartz (42.75° -RYC) plate with the 30μ transducer period. The first mode corresponds to the SAW and actually represents two modes at the same frequency, one

corresponding to the SAW on the upper surface and one to the SAW on the lower surface. Note that the SAW is the dominant mode for most RYC orientations (-50° to $+80^\circ$). The modes between 110 MHz and 166 MHz are predominantly shear vertical modes. The modes at approximately 170 MHz correspond to the fast shear wave and a leaky SAW solution associated with it. The lower amplitude modes between 170 and 190 MHz are the predominantly SH modes described by Ricco and Martin. The coupling strength of these modes increases as the plate is thinned. The modes above 190 MHz are compressional modes.

The concept of a leaky SAW deserves clarification. A leaky SAW is a generalized Rayleigh-type mode that typically consists of a mixture of compressional, shear vertical and shear horizontal displacements that are trapped to the surface. (Typically, pure-SH leaky-SAW modes radiate energy parallel to the surface and form "pure SH-SAW solutions, as in 36° Rotated Y-cut lithium tantalate). The trapped wave cannot satisfy the stress-free boundary conditions at the crystal surface by itself and the residual stress is balanced by the radiation of a bulk acoustic wave into the crystal. The radiated (leaked) energy introduces a propagation loss to this mode in an infinitely thick crystal. In a finite plate, the radiated energy is reflected back and a leaky-SAW derived APM results. Typically, the radiated / reflected wave cannot satisfy the stress-free boundary conditions by itself and a secondary trapped wave exists on the opposite surface of the crystal. Based on observation, there appears to be at least two of these modes associated with the fast shear and compressional bulk acoustic waves for most orientations and thicknesses. In these cases, the leaky-SAW is closely related to a particular bulk wave and the associated APMs seem to always come in symmetric and asymmetric modes (the trapped waves obey $\cosh()$ and $\sinh()$ functions).

ST-Quartz APM Electrical Efficiency vs Frequency

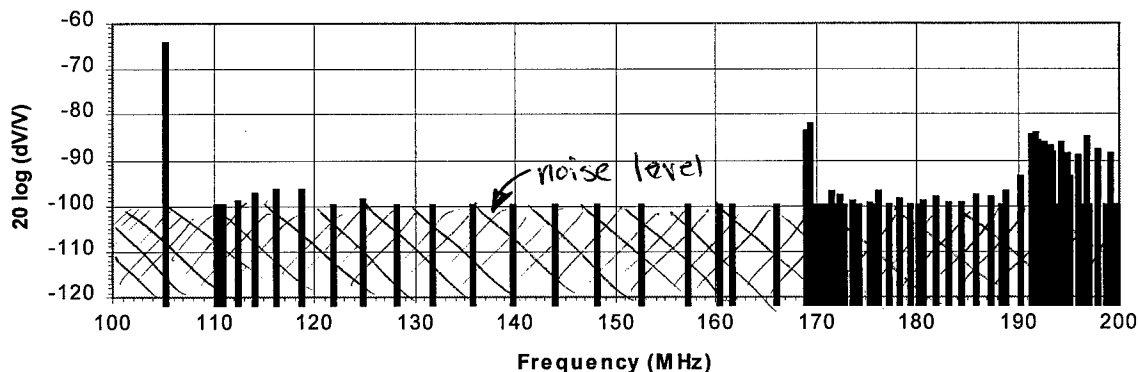


Figure 16. APM spectrum for ST quartz using 0.5 mm thick plate with 30 micron IDT period. The spectrum consists of the SAW at 105 MHz and three clusters of APMs. The group between 110 MHz and 170 MHz derive from the slow shear wave. The modes at 170 MHz up to 190 MHz are closely related to the modes in Figure 1 and were employed by Martin et al. The modes above 190 MHz are discussed below.

II.B.3.c) The Slow Shear Bulk Wave for X-propagating Rotated Y-Cut

Other orientations might offer better properties. In fact, there are an unlimited number of potential plate orientation directions and propagation directions within a crystal; however, manufacturing and device physics issues favor maintaining either the plate normal or the propagation direction along a major crystalline axis. Since the most piezoelectrically active orientations of quartz are those with plate normal near the crystalline Y-axis and propagation along the crystalline X-axis, we have focused on the X-propagating rotated Y cuts (RYC) of quartz. A variety of APM properties may be obtained by examining these orientations. The properties of these orientations are determined by the superposition of three bulk acoustic

waves, namely the slow and fast shear waves at 3.29829 mm/ μ s and 5.09981 mm/ μ s and the compressional wave at 5.74443 mm/ μ s. Typically, there is a cluster of APMs associated with each of these bulk wave velocities which primarily derive their properties from a mixture of the associated bulk wave and those with slower velocities. Plate modes based on the slow shear wave exhibit relatively constant properties as a function of the plate orientation. They are characterized by low electrical efficiency and a 10 to 20 ppm/ $^{\circ}$ C temperature coefficient. The wave motion of the bulk wave is polarized $\sim 25^{\circ}$ from the crystal's Y-axis (away from Z). Thus, for the 25° -RYC orientation, the waves are pure shear-vertical (SV) and cannot be fluid loaded.

For orientations near -65° -RYC, the waves are essentially pure SH. This orientation does not provide a substantially more useful alternative, despite the pure SH behavior. The coupling for this mode is even lower ($k^2 = 0.000022$) and the temperature coefficient of frequency (TCF) is 15 ppm/C. The mass sensitivity is approximately -0.75 ppm- mm^2/ng , which is acceptable, but lower than desired. Individual modes cannot be resolved without long transducers (>250 periods). The slow shear modes offer neither a single nor a temperature stable mode.

II.B.3.d) Acoustic Plate Modes Based on Compressional Bulk Waves

Under prior funding, we examined a group of APMs that we thought to be predominantly SH. These modes correspond to the group above 190 MHz in Figure 16. More careful modeling indicates that these modes are not SH, but rather are a specific case of generalized APMs that has received little prior attention. These waves do have low acoustic displacement perpendicular to the surface and thus radiate little acoustic energy into the fluid; however, the primary component of surface displacement is along the propagation direction, not transverse to it. These longitudinally polarized APMs are also capable of propagating in contact with a fluid and are a candidate for use in the proposed sensor. The generalized APMs exist for all rotated Y-cut (RYC), X-propagating cuts of quartz and predominantly longitudinal waves exist for all of these orientations based on the compressional wave at 5.74443 mm/ μ s. In general, it is difficult to base an oscillator on a single acoustic mode since there are a large number of closely related modes with similar electrical efficiency. However, two modes become dominant between 15° and 30° -RYC.

We attempted to employ these modes on 23° -RYC quartz with very limited success. Even on thinned plates (0.1 mm) using 30μ transducer periods and 120 period transducers, we were unable to completely resolve the individual APMs. As an added complication, the APMs are strongly dominated by the SAW mode on the IDT surface. Although it is possible to damp the SAW mechanically, this introduces additional sources or random variation to the APM phase / frequency as well. Finally, the temperature coefficient of frequency was measured as -15 ppm/ $^{\circ}$ C, as reported last month.

The inability to resolve individual modes led to detrimental behavior, since the two modes are of opposite symmetry, as discussed above. That is, one mode has even symmetry with respect to the center of the plate while the other has odd symmetry. If the two modes are electrically generated with approximately equal amplitudes (and equal phases) on the IDT surface, it follows that the waves will have equal but opposite amplitudes in the lower surface. This results in little or no acoustic displacements on the fluid loaded surface and therefore in little or no sensitivity to mass loading.

We have performed a thorough numerical analysis of the compressional mode APMs in rotated Y-cut quartz. The dominant APM (evaluated within the family of compressional modes only) is expected to provide zero temperature coefficient for both -25° -RYC and $+15^{\circ}$ -RYC. The former orientation has excessive attenuation (1 dB/mm) and low electrical efficiency ($k^2 = 0.00012$) with a mass sensitivity of approximately 1.5 ppm- mm^2/ng . The latter orientation offers an attenuation of 0.36 dB/mm and a coupling of 0.0002 with similar mass sensitivity.

II.B.3.e) Acoustic Plate Modes Based on the Fast Shear Bulk Wave

While the compressional APMs represent a novel approach, the fast shear APMs also deserve further attention. While the slow shear mode provides undesired shear vertical APMs for orientations near 25°-RYC, the fast shear provides shear horizontal APMs near this orientation. In fact, leaky-SAW derived SH modes exist below 25°-RYC and traditional sinusoidal-based SHAPMs (as described by Martin) exist above 25°-RYC. A detailed numerical study of the dominant fast shear derived APMs indicates that temperature stable modes exist near ST-cut (42.75°) and near 15°-RYC. The transition from negative to positive temperature coefficient near ST was abrupt and may correspond to a change in the dominant mode rather than a temperature stable orientation. Martin et al. report no stable SHAPM near ST-quartz. The expected properties of the 15° cut are: $k^2 = 0.0002$, attenuation of 0.12 dB/mm and a mass sensitivity of -2 ppm-mm²/ng. For 0.5 mm thick plates, the leaky-SAW derived (cosh and sinh) modes are dominant. In order to resolve these modes, one requires a 300 period (9 mm) long transducer with 30μ period on a 0.5 mm plate. This device geometry is not possible with the existing packages, nor is it consistent with the goal of minimizing the device size. The required chip size would exceed 1" in length. Furthermore, propagation losses would prevent proper operation of such a long device.

The problem of mode resolution may be overcome by employing thinner plates; however, the compressional APMs gain coupling efficiency faster than the fast shear modes and become dominant, yet indistinguishable. In this limit, the compressional APMs exhibit higher coupling efficiency than the fast shear modes; however, the SAW still exhibits over four times the coupling of the APMs. BIODE fabricated devices on 15°-RYC using an existing electrical design with 125 period transducers; however, the resulting devices were not useful.

II.B.3.f) Summary of APMs Derived from Specific Bulk Acoustic Waves

To summarize the results discussed so far, 15° rotated Y-cut quartz is predicted to support temperature stable APMs derived from two separate leaky-SAW modes closely linked to the onset of a specific bulk wave (fast shear and compressional waves). These leaky-SAW modes are closely tied to the fast shear and compressional bulk acoustic waves. The APMs are electrically dominated by the SAW, which propagates on the transducer surface and does not contribute to mass detection. The SAW may be rejected by employing phase bridge techniques or by employing external electronic filtering. The leaky-SAW derived modes discussed thus far tend to provide at least one symmetric and one anti-symmetric plate mode, making it difficult to excite a single acoustic mode. Finally, the electrical coupling of the candidate APMs is not a substantial improvement over the pure-SH modes of AT-90.

II.B.3.g) APMs Derived from an Independent Leaky SAW

At this point, it proves instructive to examine the properties of ZX-lithium niobate and to inquire why they occur. This substrate provides a single, electrically dominant acoustic plate mode which is predominantly SH at the surface. The APMs in this orientation are derived from a leaky-SAW which is not closely related to a single bulk wave, but rather represents a unique mixture of the constituent bulk waves. When the leaky SAW is closely related to a single bulk wave, spectra resembling that demonstrated in Figure 14 are the most common. This classic behavior occurs when the bulk wave almost satisfies the boundary conditions by itself and the leaky SAW solution is a very slight modification of the bulk wave. When slightly stronger modifications of the bulk wave are required to satisfy the boundary conditions, spectra such as Figure 16 occur. However, under certain symmetry conditions, a strong leaky-SAW exists which is relatively independent of the individual bulk waves.

This behavior occurs for -75°-RYC, which is known as the leaky-ST cut (LST) of quartz. The free surface of an extremely thick plate (relative to an acoustic wavelength) supports a

second Raleigh wave which radiates very little energy into the crystal. The primary Raleigh wave has very low electrical coupling and the second is the dominant mode. The temperature stability of the mode is exceptional until metal loading is considered. Under this condition, the material behaves like ST-quartz with a parabolic frequency vs. temperature behavior. Even in finite thickness plate, the acoustic energy is strongly trapped to the transducer surface.

This strongly trapped acoustic wave is a singular behavior of the LST cut and slight modifications to the plate orientation dramatically increase the amplitude of the SH standing wave. Unfortunately, they also introduce non-SH displacements into the standing wave which lead to additional fluid loading propagation losses. The APM derived from the leaky-SAW is predicted to be temperature stable at -73° and -65° rotated Y-cut. The former orientation has minimal amplitude of the standing wave. The latter orientation has useable properties, namely the electrical coupling, k^2 , is 0.00064, the propagation loss is 0.65 dB/mm and the mass sensitivity is $-0.6 \text{ ppm}\cdot\text{mm}^2/\text{ng}$.

The mode spectrum for the selected orientation is given in Figure 17. Note that the SAW solution at 110 MHz and the family of slow shear derived APMs between 110 and 150 MHz have negligible electrical efficiency, with the exception of the five or six modes derived from the independent leaky-SAW. Note also that the dominant mode, discussed above, has nearly approximately five times the k^2 value of the next most strongly coupled mode. Finally, note that the mode is mostly resolved by a 125 period transducer length. Other clusters of APMs associated with the fast shear and compressional wave exhibit tolerable electrical efficiency but are not SH modes and suffer high propagation loss.

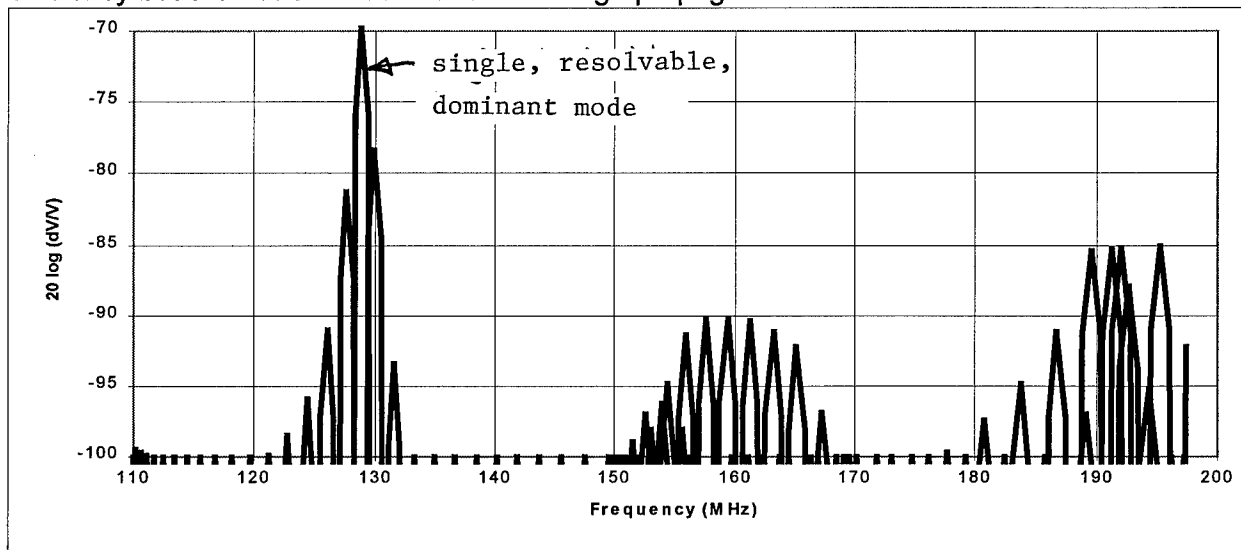


Figure 17. APM spectrum of -65° -RYC quartz with 125 transducer periods, 30 micron period and 0.5 mm plate thickness. Although the mass sensitivity of the dominant mode is $1/8^{\text{th}}$ the value of ZX lithium niobate for the same design parameters, the temperature stability should lower the noise floor by as much as 40 times, yielding a five-fold improvement over lithium niobate in minimum sensitivity.

Traditionally, the expectation has been that the thinner the plate thickness, the more sensitive the APM will become. However, this is theoretically not the case for the current mode. Until the thickness approaches two periods (0.060 mm in this case), the APM properties remain very consistent. Below this thickness, the properties are very erratic. If the transverse resonance conditions are carefully adjusted, it is possible to obtain a well-coupled mode with high mass sensitivity (-3.5 to $-4 \text{ ppm}\cdot\text{mm}^2/\text{ng}$) and low loss (0.35 to 0.45 dB/mm). This theoretically occurs for 0.030 mm thickness plates. However, if the transverse resonance conditions are not perfectly balanced, the non-SH displacements dominate and the propagation loss is extremely high (1 to 2 dB/mm).

Another approach to increasing the mass sensitivity is to increase the operating frequency (decrease the transducer period). While the spectrum (not shown) for a 10μ period and 0.1 mm plate thickness provides a single mode, the attenuation of the wave is excessive. Thus, the optimum conditions for this wave appear to be the assumed 30μ IDT period on a 0.5 mm thick plate. While thinner plates will obtain some sensitivity increase, the gain is not worth the additional processing to thin and polish the individual crystals.

II.B.4) Lithium Tantalate Shear Horizontal Acoustic Plate Mode (SHAPM)

II.B.4.a) Approach for the Orientation Search

The quartz effort began with the knowledge that piezoelectric effects were strongest for X-propagating rotated Y-cut (RYC) crystals of quartz. More extensive searches could be performed; however, historical evidence indicated that these orientations would be the most promising. Little historical data is available on lithium tantalate (LTA). It is known that 36° RYC LTA supports an SH-polarized SAW solution.

In order to overcome the lack of prior experience and still efficiently screen the material, an innovative approach was employed to locate electrically efficient, shear horizontal APMs with the potential for a single dominant mode. The effective dielectric constant of a piezoelectric surface relates the spatial distribution of charge and electric fields. In the Fourier domain, this relationship is a function of the frequency, ω , and the spatial wavenumber, k . The numerical calculation of the effective dielectric constant is simple and efficient and may be expressed as a function of the acoustic velocity, $v=\omega/k$. At velocities corresponding to wave propagation on a metal-plated surface, there is charge in the absence of electric field and the function is infinite (pole). At velocities for which a wave travels on an electrically free surface, the function is zero. Losses, such as the radiation of energy into an adjacent fluid, damp the pole and zero. The electrical efficiency is related to the separation between the pole and the zero for a given mode.

Effective dielectric constant was plotted for a piezoelectric surface both with and without ideal water (no viscosity, no shear elasticity) in contact. Pure shear modes are unperturbed by this loading, while pure Rayleigh modes are completely attenuated. Variations of the three Euler angles defining a surface normal and propagation direction were considered on an angular grid for the rotated Y' axis and propagation direction. Rotated Y, YX and X cuts were analyzed.

II.B.4.b) Generalized Rotated Y-cut (RYC) Orientation Search

Rotated Y-cut (RYC) (IEEE standard, ZX/tlt/(0, $90^\circ+\theta$, ψ) offers many shear wave solutions. Orientations such as (0, 15, 30) offer SHAPM spectra similar to Figure 14. Based on experience, these spectra are undesirable. This characteristic slowly develops into the familiar spectrum of ZX lithium niobate at (0, 0, 0) and to a similar spectrum towards (0, 90, 0). Orientations of the type (0, θ , 90) have both plate normal and propagation axis in the crystalline YZ plane. This plane of mirror symmetry can only support piezoelectric coupling to Rayleigh waves. Thus, optimal shear wave solutions should be expected far closer to (0, θ , 0). Numerical analysis of the effective dielectric constant supports this. Optimal behavior is observed between (0, 90, 0) and (0, 165, 0).

These orientations were analyzed using acoustic plate mode (APM) theory. For completeness, APM properties were evaluated over the range $0 \leq \theta \leq 180$ and $0 \leq \psi < 60$. Diffraction and power flow effects are undesirable for $\psi \neq 0$. For the X-propagating ($\psi = 0$) orientations, the temperature coefficient of frequency (TCF) is given in Figure 18, repeated from the proposal. As discussed previously, the best temperature stability occurs between 90° and 150° (0° and 60° for θ). TCF is optimized near $\theta=15^\circ$ (105°), as is the ability to isolate a single acoustic mode. However, neither factor is sufficient reason to employ a custom orientation, especially given an additional reduction in mass sensitivity. Figure 19 shows the variation of

TCF for different propagation directions on Y-cut LTA. Generally, X-propagating orientations are superior. Based on these results, YX is the best RYC orientation of lithium tantalate in terms of performance / economics tradeoffs.

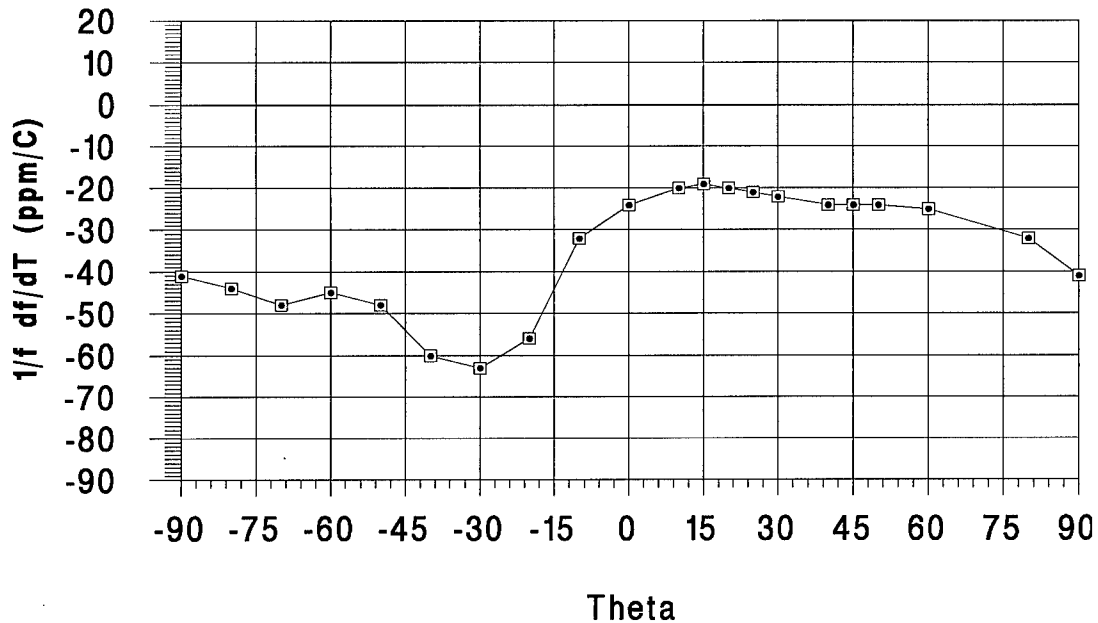


Figure 18. Temperature coefficient of frequency (TCF) for the rotated Y-cuts of lithium tantalate. Theta in the figure is (0-90) and indicates the deviation from Y-cut. Variations in IDT period alter the TCF near 15°, which can be as small as 10 ppm/°C.

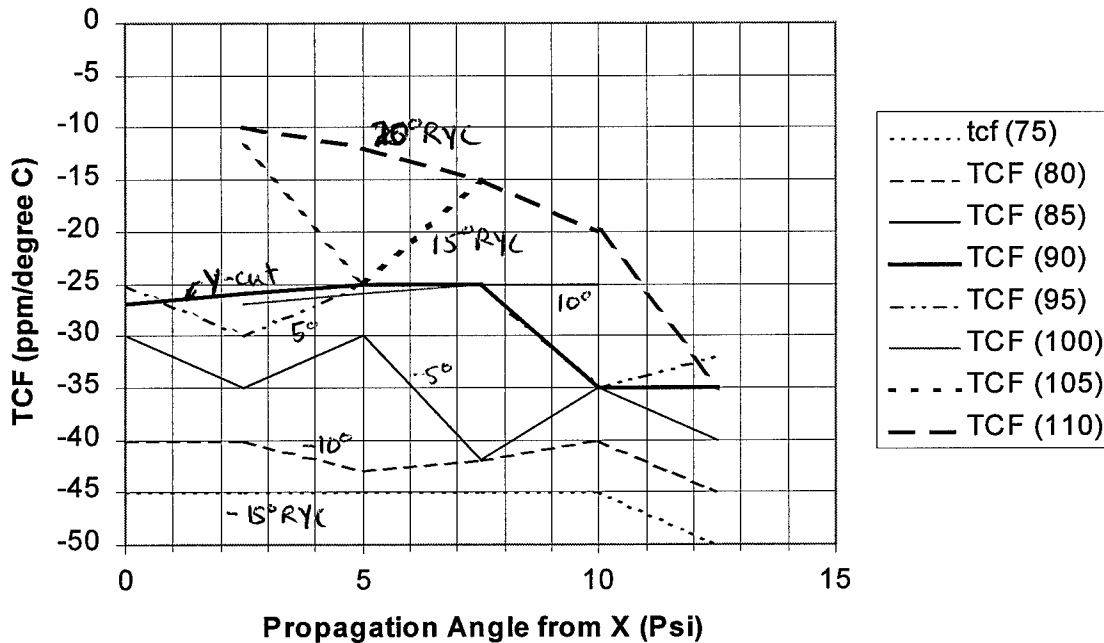


Figure 19. Changes in TCF as propagation direction is varied for different RYC wafers in the range $75^\circ \leq \theta \leq 110^\circ$. Generally, TCF becomes worse as the propagation angle becomes nonzero. The numbers in parenthesis are θ .

II.B.4.c) Generalized Rotated X-cut (RXC) Orientation Search

Rotated X-cut (RXC) (IEEE standard ZX/tlt/(90, 90+ θ , ψ) also offers shear wave solutions for Y-axis propagation ($\psi=0$). At approximately -40° RXC and -20° RXC with propagation -30° from Y, these solutions appear to evolve into an STW mode based on the effective dielectric constant plots. Finally, some shear modes are detected on X-cut (90, 90, ψ) wafers; however, experimental devices on X-cut have been unsatisfactory.

RXC LTA exhibits temperature compensated APM solutions; however, these are Raleigh modes and will not operate with liquid loading. Finally, the APMs are typically dominated by the SAW on RXC orientations and no single, dominant APM exists. Based on these calculations and prior experimental data, RXC orientations have been eliminated.

II.B.4.d) Generalized Rotated YX-cut (RYXC) Orientation Search

While there are any number of potential choices other than rotated Y-cut and rotated X-cut, device design and operation is aided by employing crystal symmetry. Thus, $\Phi=45^\circ$ was selected as a third orientation family for careful consideration. These orientations begin as Z-cut for $\theta=0^\circ$ and become $\frac{1}{2}(X+Y)$ surfaces at $\theta=90^\circ$. Orientations near (45,40,0) exhibit a high quality shear mode that should behave similar to 36° degree RYC (0, 126, 0). Perturbation of this mode towards (45, 90, 0) offers similar spectra to (0, 90, 0); however, with a stronger SAW mode and on a more complicated orientation. APM analysis did not reveal dominant modes in these cases, however. In general, RXYC orientations exhibited problematic power flow angle problems, wherein acoustic energy would travel at an angle to the intended direction. No orientation provided any improvement over RYC orientations. The only temperature stable orientations were predominately Raleigh and unsuitable to the proposed application.

II.B.4.e) Modeling of Candidate Devices

Computer modeling of a suitable lithium tantalate (LiTaO_3) compromise orientation is complete and has provided encouraging results. We have further modeled the properties of SHAPMs near Y-Cut X-propagating and the results confirm the initial data discussed last month. The anticipated temperature coefficient of frequency (TCF) is -25 ppm/ $^\circ\text{C}$. BIODE has performed computer modeling of candidate device structures based on this orientation. BIODE ordered eight wafers of X-propagating Y-cut (YX) from Sawyer Crystal Products. BIODE received eight wafers of X-propagating rotated Y-cut (RYC) from Sawyer Crystal Products in April. Long lead times were incurred due to the tight global market for piezoelectric substrates in wireless communications. The wafers were sent to other service providers for backside polishing and metalization.

One design is a low-Q delay line (time-frequency product of 40, nominal phase shift of $40 \times 360 = 14,400$ degrees) with a center frequency of 63 MHz. The primary advantages of this design are that four devices may be built on a single chip in existing packages and that the electrical design is very simple. The sensor is very similar to early lithium niobate designs and is expected to provide similar electrical efficiency and mass sensitivity with improved temperature stability. The results of a SAW model of the device (for the dominant SHAPM) are given in Figure 20. Measured electrical properties are given in Figure 21, and indicate that the adjacent mode suppression is unacceptable for reliable sensor applications.

Other device designs have been simulated and will be considered in light of the experimental results on the first design. The second design employs a lower design frequency in order to provide improved isolation of adjacent modes. The drawback is that it can only offer two devices per chip in the current packages. The third SHAPM design assumes that the mode isolation can be made adequate at 62.5 MHz and employs a resonator structure to improve the sensor Q (frequency resolution). Again, only two devices per package will be possible. In light of oscillator results (Section II.C.2) more than two devices per package may be undesirable.

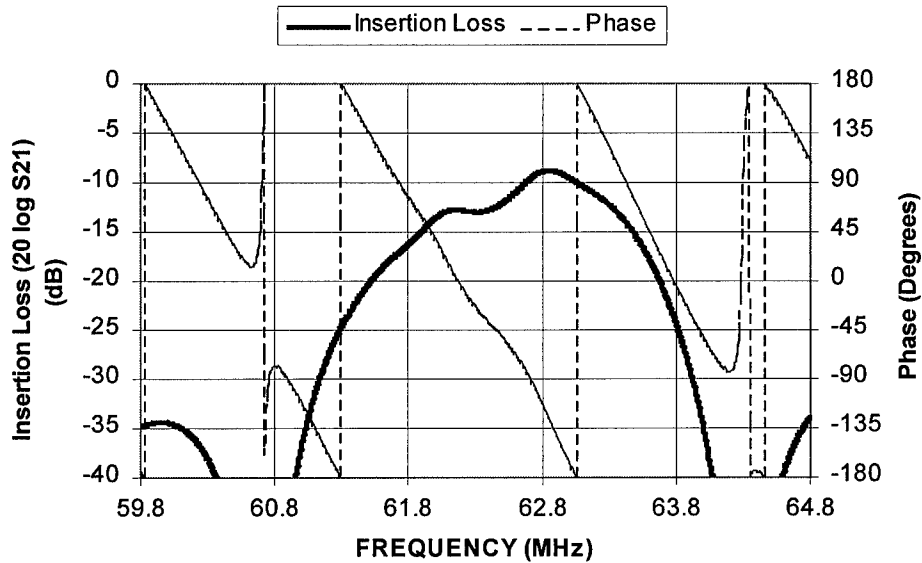


Figure 20. Modeled properties of the YX lithium tantalate SHAPM at 63.5 MHz. A single point exhibits less than -20 dB of insertion loss and 180° phase simultaneously (~ 63 MHz). In fact, all phase values between 0° and -180° are unique in that there is only one frequency for which the device exhibits less than 20 dB of insertion loss. This behavior is desirable for oscillator applications.

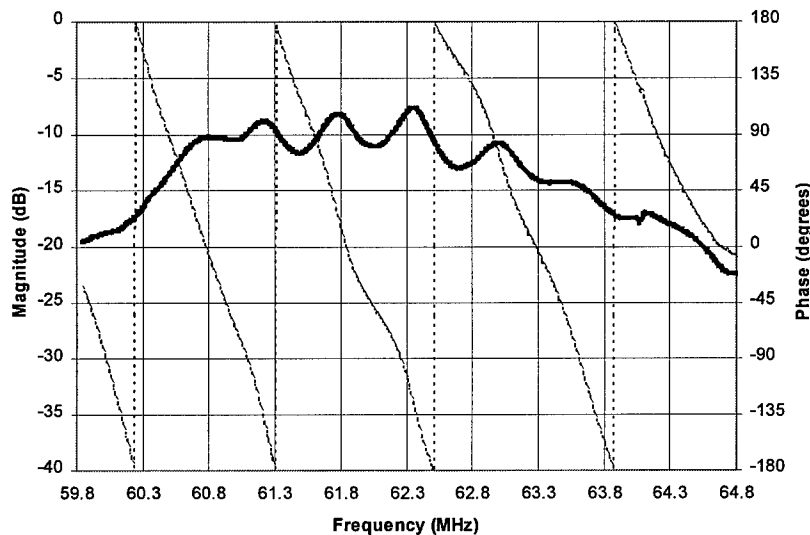


Figure 21. Measured properties of the YX lithium tantalate SHAPM indicating that the adjacent plate modes (a total of four modes) are indistinguishable in this design. Oscillator circuits do operate on the desired SHAPM; however, oscillator noise performance is degraded by the adjacent modes and reliability is poor.

II.B.4.f) Measurement of Prototype Devices

BIODE has tested the initial prototypes of delay line structures with an operating frequency of 62.5 MHz. The chips implement a four sensor array with an on chip serpentine resistor. The design provided suboptimal rejection of adjacent modes. Nonetheless, viscous liquids were employed to measure the mass sensitivity of the devices. The predicted sensitivity was -0.82 ppm- mm^2/ng while measured values ranged from -0.4 to -0.6 ppm- mm^2/ng . In a

single experiment, a sensitivity of $-0.8 \text{ ppm}\cdot\text{mm}^2/\text{ng}$ was measured, indicating that surface slippage may have slightly lowered the loading due to viscous liquids in the other experiments. The fact that 50-65 MHz LTA SHAPMs offer the same sensitivity as 193 MHz quartz SHAPMs (Table 3) raises a substantial engineering decision. LTA has approximately 10 times the temperature coefficient of frequency. Initial attempts to calibrate the temperature effects have been reasonably successful; however, this technique could be applied to quartz with even better results. Electrical efficiency is excellent for lithium tantalate and the four-fold reduction in frequency results in a 16-fold reduction in power dissipation in any associated CMOS circuitry. This decision will be reached in the next quarter.

II.B.5 Quartz STW (partially supported by DAAM01-95C-0076)

In order to understand the behavior of STW devices, simulation software for SAW resonators was applied to the STW structure. While not entirely applicable, this software does predict the salient features of the STW device. The key parameters of the STW may be divided between structural (geometric) parameters and material parameters. The structural parameters were determined by design and are summarized in Table 4, below. Figure 22 illustrates the meaning of each parameter. Note that the electrical period is twice the electrode periodicity, since alternate electrodes have opposite polarity. The key features of the resonator that are affected by each parameter is indicated.

Parameter	Value	Dependent Features of Resonator
Periodicity of the electrodes (p)	5.6μ	Center frequency ($v/2p$) and size ($\sim p^2$)
Number of reflector electrodes (N_r)	500p	Resonant Q ($f_0/df \sim N_r$) and loss
Number of IDT electrodes (N_i)	101p	Electrical efficiency (loss) and loaded Q
Offset of IDT from reflector (dN)	0.25p	Electrical eff. and frequency offset.
IDT separation (N_s)	12p	integer to satisfy resonance.
Device Width (W)	.81 mm	Electrical efficiency, input impedance
Metal thickness (h)	0.25μ	see material parameters

Table 4. The structural parameters of the STW resonator.

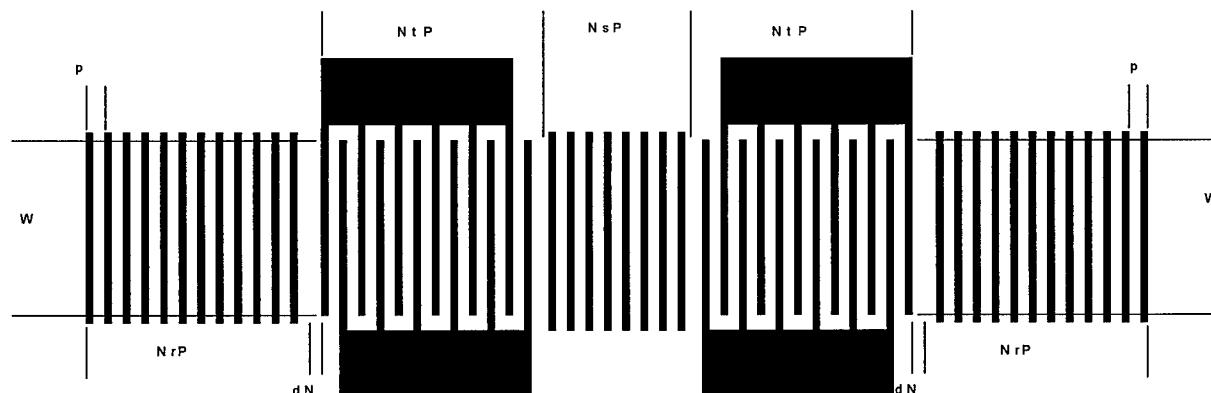


Figure 22. Structural configuration of the STW resonator.

Some of the material parameters - such as acoustic wave velocity, capacitance of the transducer, piezoelectric coupling strength and mechanical reflectivity - are weak functions of the structural parameters. During the initial design, these values are estimated and then verified experimentally. For example, the STW velocity is slightly perturbed from the bulk wave velocity ($\sim 5090 \text{ m/s}$) and is only slightly lower. The effective capacitance per electrode pair per unit width depends on the ratio of the electrode widths to the space between them and is

approximately .04 pF / mm per electrode pair. The piezoelectric coupling is independent of metal thickness for a SAW but has a complicated dependence on both metal thickness and the difference between the operating and center frequencies for the STW. The STW has very little coupling in the limit of thin transducer metal but becomes more strongly coupled as the wave is trapped to the surface. For a SAW, the mechanical reflectivity is linearly related to the metal thickness; however it increases super-linearly (possibly quadratic) with metal thickness as wave trapping occurs. Table 5 presents the assumed values that were employed in modeling the device.

Parameter	Value	Dependent Features of Resonator
Acoustic Velocity (v , meters/s)	5090	Center frequency ($v/2p$) \sim 454.46 MHz
Norm. capacitance (C_o , pF/mm)	.04	Input impedance $\sim 1/(C_o N_t W(k^2 + j\omega))$
Piezoelectric Coupling (k^2)	.0008	Electrical efficiency.
Mechanical Reflectivity (κ/λ)	.01	Resonant Q, resonant frequency.
Mechanical losses (γ/λ)	.001	Resonant Q, electrical efficiency.

Table 5. The approximate structural parameters of the STW resonator assumed for the initial design modeling.

Figure 23 presents the modeled electrical response of the device, as designed. The predicted resonance is sharp (has a high Q factor or narrow bandwidth) and occurs at 454.77 MHz, slightly below the center frequency of the IDTs. The predicted insertion loss is approximately -8.66 dB, which is an excellent electrical efficiency.

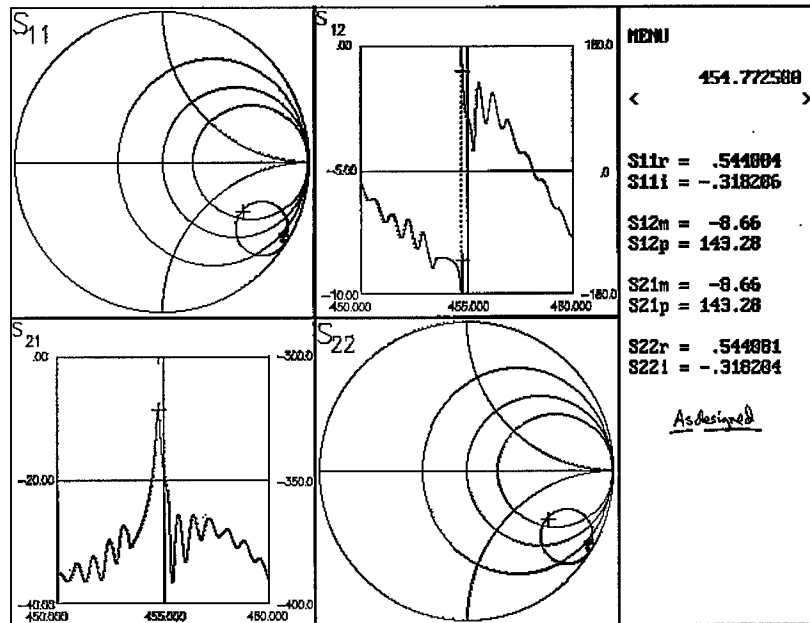


Figure 23. Predicted device response for the BIODE / ARL STW resonator.

The predicted response of Figure 23 should be compared to the measured response of the bare, air loaded device in Figure 24. There are several major discrepancies between the two responses, most notable of which is the relationship between the resonant frequency and the center frequency of the IDT responses. While the prediction was that the resonance would be slightly below the center frequency, the actual device exhibited resonance well below the center frequency. Two device parameters could have altered the resonant frequency, namely the IDT offset from the reflectors, which is not material dependent, and the mechanical reflectivity, which is.

The resonance location is not strongly influenced by the magnitude (strength) of the reflection coefficient, but is strongly dependent on its phase. For the SAW on symmetric orientations (such as ST-quartz), there is no phase shift, *per se*. A given electrode material has either positive or negative reflections, dependent on its density and stiffness. However, the current substrate orientation is not symmetric, nor is the device employing a SAW. Therefore, the phase of the reflectivity (relative to the piezoelectric coupling) may have an arbitrary value, which is primarily dependent on the substrate orientation. The amount of phase shift is traditionally measured such that 90° of phase shift is the same as a negative number. This occurs since the reflected wave travels through the phase shift twice. Materials with a reflectivity phase shift of +/- 45° have unique properties, in that the interdigital transducer is no longer bidirectional. When a voltage is applied to the transducer, the acoustic energy is preferentially radiated from one of the two ends of the transducer. This effect has been applied to low loss delay lines, where it may be employed to lower the insertion loss of the devices.

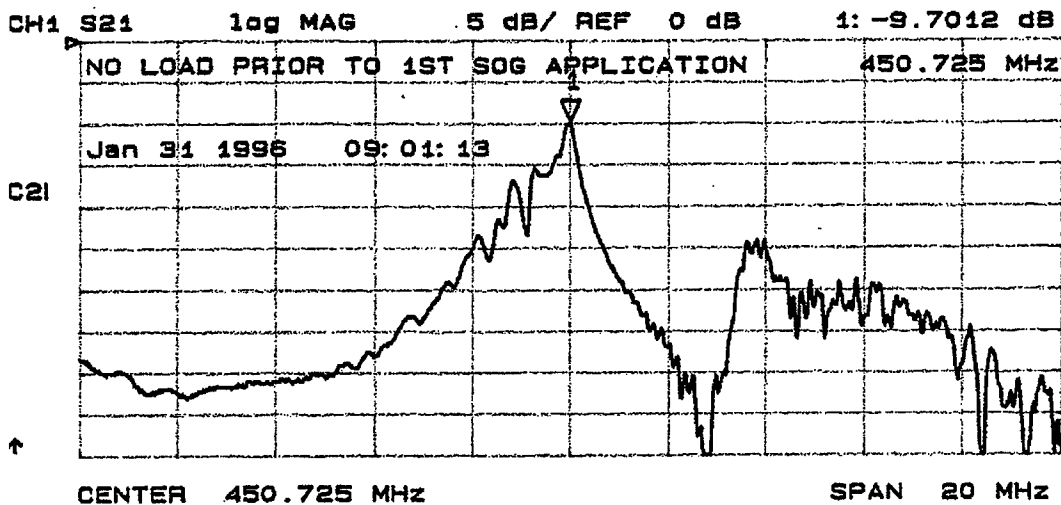


Figure 24. Electrical response of the resonator with a 2,000 Å sputtered SiO₂ layer. The marker indicates the resonance peak at 450.725 MHz having -9.7 dB of attenuation. The SiO₂ contributes unwanted plastic losses, which lower the quality of the resonance and increase the propagation losses.

The situation in a resonator is somewhat more complicated. The synchronous array of reflective electrodes trap the acoustic wave and provide a standing wave pattern. The offset phase between transduction and reflection determines the optimum placement for the transducer relative to the reflectors so that the electrodes will be placed at the peaks of the standing wave. An unexpected phase shift can lead to improper placement of the electrodes with respect to the standing wave and can have serious impact on the device response. For certain device geometries and phase angles it is possible to completely decouple the resonance from the transducers, providing no electrical response at the resonant frequency. This in fact occurred for the back-up design (not shown). Figure 25 presents the modeled response of the device adding a 45° phase shift of κ . Qualitative agreement is seen between the measured and modeled responses. The primary difference between the responses is the lower insertion loss (higher electrical efficiency) of the measured device below the resonance and the lower level of periodic ripple in the periodic response. A higher value of the mechanical loss would account for the reduction in ripple and also of the resonant Q. A higher (frequency-dependent) value of the piezoelectric coupling would account for the higher electrical efficiency off-resonance and compensate for the added losses caused by the mechanical damping. Additional modeling was performed and indicates that the coupling and mechanical losses are both slightly underestimated. This information will be extremely useful in designing second generation STW

devices. Before a second design is performed, the materials issues of the thick film must be addressed. This will be addressed in early FY2.

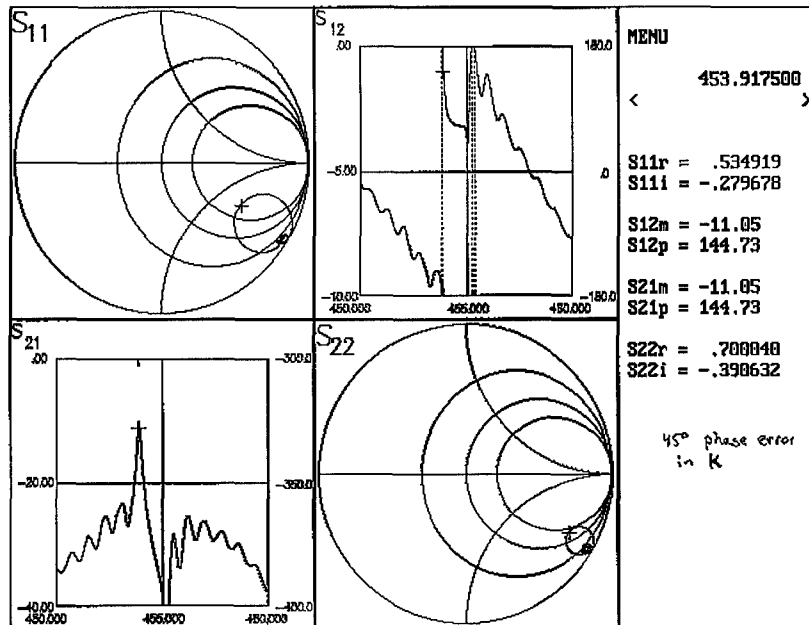


Figure 25. Modeled electrical response with 45° of phase shift in the mechanical reflectivity. The decrease in resonant frequency is in good agreement with the measured response. Slightly larger decreases may be obtained as the phase angle approaches 90° , at which point the resonance will disappear. Note that the input and output transducers have different electrical properties, indicating that the input transducer is more closely positioned on the standing wave peaks than the output transducer.

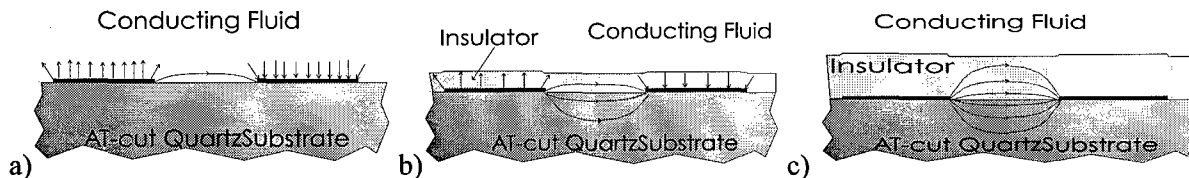


Figure 26. The IDTs optimally consist of equal line and space dimensions (e.g. 2.5μ) and employ relatively thin aluminum metallization (e.g. 1500\AA). (a) Chemical passivation via a $500 - 1500\text{\AA}$ thick dielectric film provides no electrical isolation between the IDTs and the conducting liquid allowing complete short-circuiting of the IDT. (b) Even films approaching 5% of the IDT period (e.g. 5000\AA) provide only partial isolation and result in some reduction of electrical efficiency. (c) When the film thickness exceeds 10% of the IDT period, electrical isolation is sufficient.

Figure 26 shows a cross-sectional view of a liquid loaded STW device coated with various thicknesses of dielectric films. One of the well-known concerns is that ions in solution will short-circuit the electrical connections. This electrical effect only influences the operation of the IDTs and is distinct from the mechanical losses induced by viscosity. This has traditionally been overcome by placing the liquid cell entirely between the input and output transducers [34,35]. While viable in the laboratory, this is not a reproducible geometry and is not compatible with high frequency sensors having small physical geometries. One approach is to apply a thin glassy film over the transducers to provide an insulating layer, as seen in figure 5.b. While the thin insulating layer protects against corrosion, it does not electrically insulate the IDTs. In fact, even non-conducting liquids will "short-circuit" the IDTs capacitively and the associated losses are proportional to the dielectric constant of the liquid. As seen in figure 5.c, the physical extent of the electric fields of the IDT is related to the electrode geometry (2.5μ at 500 MHz on AT-90

quartz). As the film thickness approaches an appreciable fraction of this value, the slope of the insertion loss with liquid dielectric constant diminishes. The degree of capacitive shorting is strongly influenced by the relative dielectric constants of the liquid (e.g. $80\epsilon_0$ for water vs. $2.4\epsilon_0$ for toluene) and the substrate ($4.5\epsilon_0$ for quartz and $40\epsilon_0$ for LiNbO_3 or LiTaO_3). While quartz is severely short-circuited by water, LiTaO_3 is not. Simple electromagnetic equations may be solved to determine the apparent capacitance due to the layer. Figure 27 presents the effective dielectric constant of a silicon dioxide layer, which is subsequently: (top) metallized, (center) loaded with water or (bottom) loaded with xylene. Note that the limit of zero thickness for air would be 0.222. Changing the dielectric material to silicon nitride or aluminum oxide changes the specific curves for water and xylene; however, the limiting value is unchanged. These materials incur a higher capacitance, overall, by a factor of approximately 2.5.

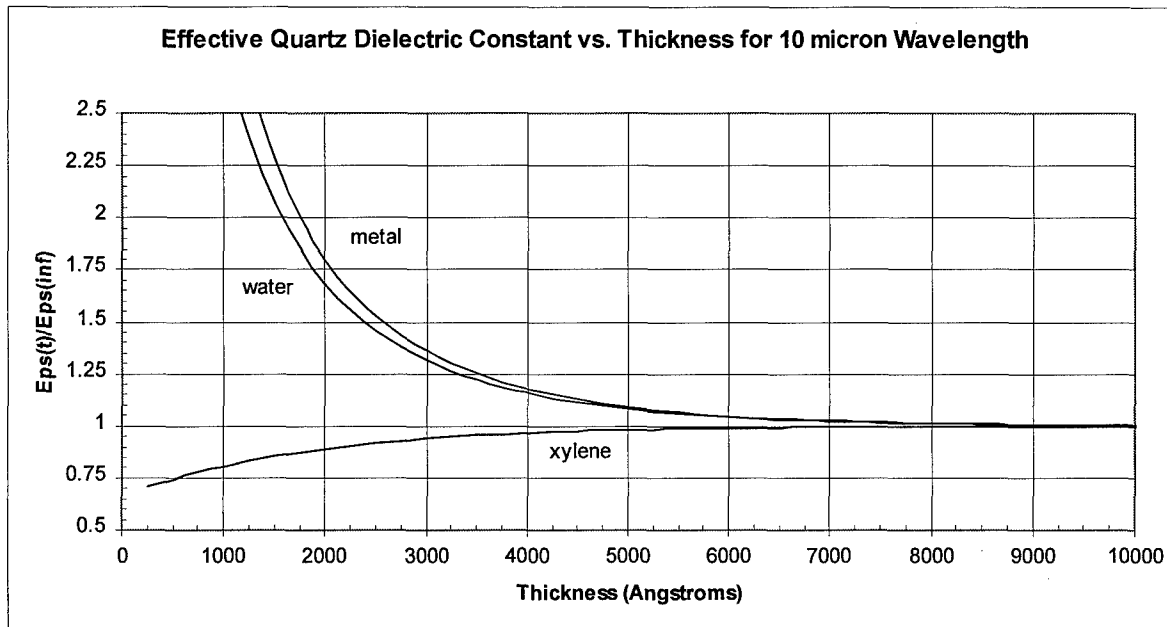


Figure 27. The effective dielectric constant of a silicon dioxide layer which is subsequently: (top) metallized, (center) loaded with water or (bottom) loaded with xylene asymptotically approaches 1. The value at which this limit is reached represents the fringing field depth of the interdigital transducer into the silicon dioxide layer. For silicon dioxide on an STW with 10μ IDT periodicity, it would be unnecessary to exceed 7000\AA .

Quartz STW resonators were coated with Si_3N_4 using plasma enhanced chemical vapor deposition (PE-CVD). STW delay line sensors were fabricated with SiO_2 films. PE-CVD Si_3N_4 films exhibited excellent mechanical properties but had pinholes that rendered them useless under fluid loading. This is not a general property of Si_3N_4 or PE-CVD, but rather was due to an arcing problem in the plasma, which led to particulate formation and film contamination. Further investigation of PE-CVD silicon nitride films is warranted and suitable service providers are being sought.

The SiO_2 films exhibited no pinholes; however, the films incur excessive mechanical losses. Efforts to anneal the amorphous films were unsuccessful. SiO_2 was deposited using pulsed DC sputtering. Recent studies using RF magnetron sputtered SiO_2 and Si_3N_4 were unfavorable. One deposition technique that provided favorable results employed electron beam evaporation of aluminum into an oxygen plasma beam. This plasma-assisted electron beam deposition technique produced high quality Al_2O_3 films. The technique is amenable to SiO_2 and perhaps Si_3N_4 with proper adaptation for silicon evaporation.

Data on the frequency shifts due to the various films is given in Figure 28. Similar shifts were expected for all three materials, although slightly lower shifts are justified for silicon nitride

due to the increased stiffness compared to silicon dioxide. The substantial velocity loading effect for RF sputtered nitride was due to low device temperature during deposition and are likely due to a high degree of viscous loading.

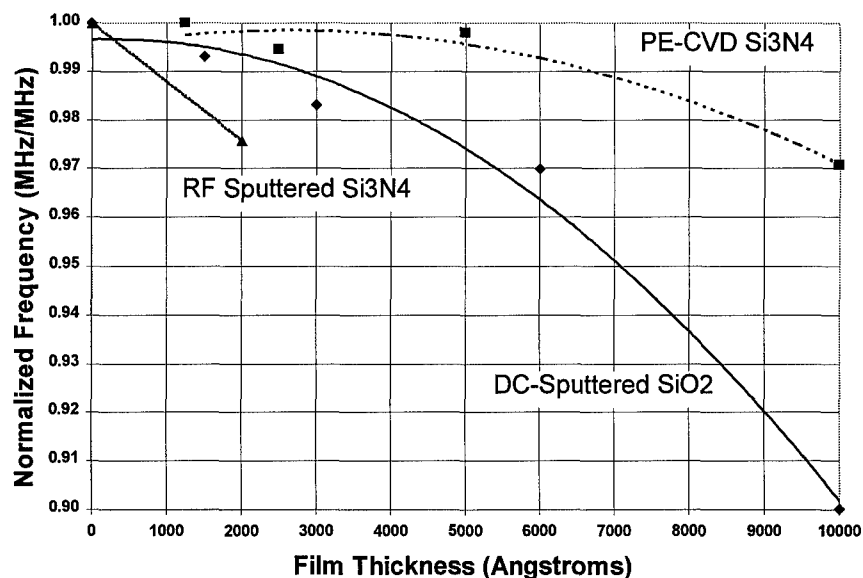


Figure 28. Frequency deviation for different dielectric layers. The plasma enhanced chemical vapor deposition (PECVD) nitride films gave the lowest acoustic losses while the RF sputtered nitride films gave the highest acoustic losses. Device temperature during deposition is known to be a substantial factor in film quality.

Liquid loaded insertion loss and frequency was measured for several liquids and thicknesses of silicon nitride (Si_3N_4). The films were deposited using plasma-enhanced CVD. The data were obtained by measuring the insertion loss for several liquids with differing viscosity and dielectric properties. The liquids employed are listed in Table 6. The values of the relative dielectric constant and the viscosity were found in 68th edition of the "CRC Handbook of Chemistry and Physics". The liquids examined were water, acetone, isopropanol, methanol, toluene and xylene. Acetone and isopropanol were employed to obtain the coefficient of viscous losses, which are indicative of mass sensitivity. These values were used to remove the viscous component of loss from the raw data. The residual loss was correlated to the dielectric constant of the liquid and the slope was evaluated. While the dielectric losses are substantially improved with respect to the uncoated devices, the residual losses were higher than theoretically predicted. The films were demonstrated to have high pinhole density, which was caused by unexpectedly high particulate formation during deposition. Dielectric shorting through the pinholes led to the relatively high losses.

Fluid	Relative Dielectric Constant	Viscosity (cp)
None	1	0
DI Water	78.54	1
Acetone	20.7	0.316
Isopropanol	20.1	1.77
Methanol	32.63	0.547
Toluene	2.438	0.59
Xylene	2.374	0.62

Table 6. Liquid Viscosity and Dielectric Data.

A delay line design was also evaluated. The nominally 500 MHz devices (IDT period = 10μ) employed closely spaced 200 wavelength IDTs. SiO_2 films were deposited using pulsed-DC sputtering and similar liquid loading experiments were performed. Figure 29 presents the slope of the insertion loss with relative dielectric constant for the two candidate geometries. Resonator structures are observed to have much less sensitivity to shorting since only a small fraction of the device is electrically active.

Figure 30 provides the information on losses due to viscosity. The delay line data exhibits predicted behavior, in which energy trapping initially increases the mechanical sensitivity until the film becomes acoustically thick ($>0.03\lambda$). As the film thickness increases, the acoustic energy is trapped to an increasingly thick surface guide and sensitivity decreases. The resonator data does not behave as expected. This may be attributed to the mechanical effects of the pinholes and to the more complex behavior of resonant structures with losses.

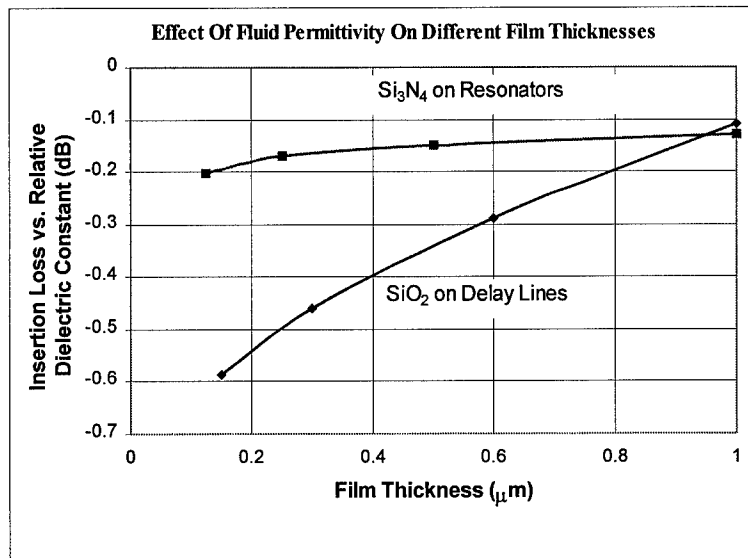


Figure 29. Slope of the measured attenuation vs. relative dielectric constant for AT-90 quartz STW resonator with various Si_3N_4 film thicknesses (upper trace) and delay lines with SiO_2 films (lower trace). The reduced shorting for resonators is due to the small fraction of device area occupied by the transducers and the existence of a 2000\AA SiO_2 underlayer.

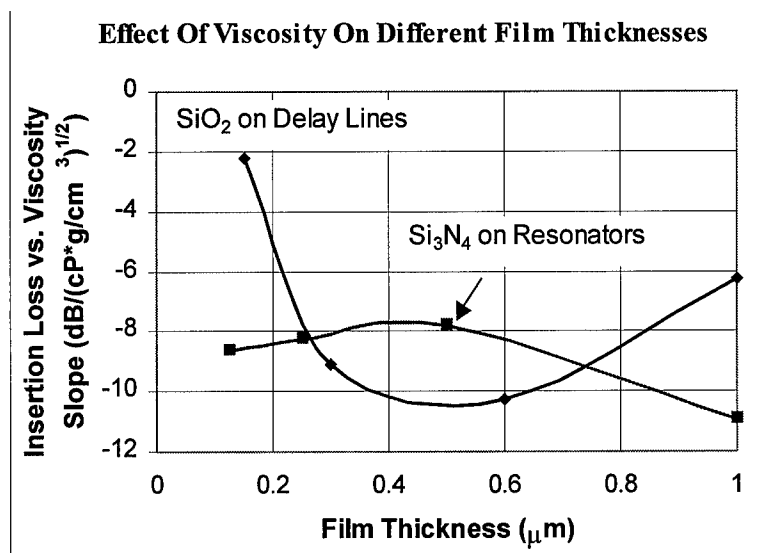


Figure 30. Slope of the measured attenuation vs. viscosity of the liquid. This slope is determined by the surface amplitudes of the acoustic wave and is directly related to mass sensitivity.

Figure 31 presents the same STW resonator's response with xylene loading. The increased insertion loss (8 dB) is attributable to a number of mechanical effects. These include defect-driven radiation of energy into liquid compressional waves, viscous losses and the reduction of the resonance peak to the direct IDT signal level.

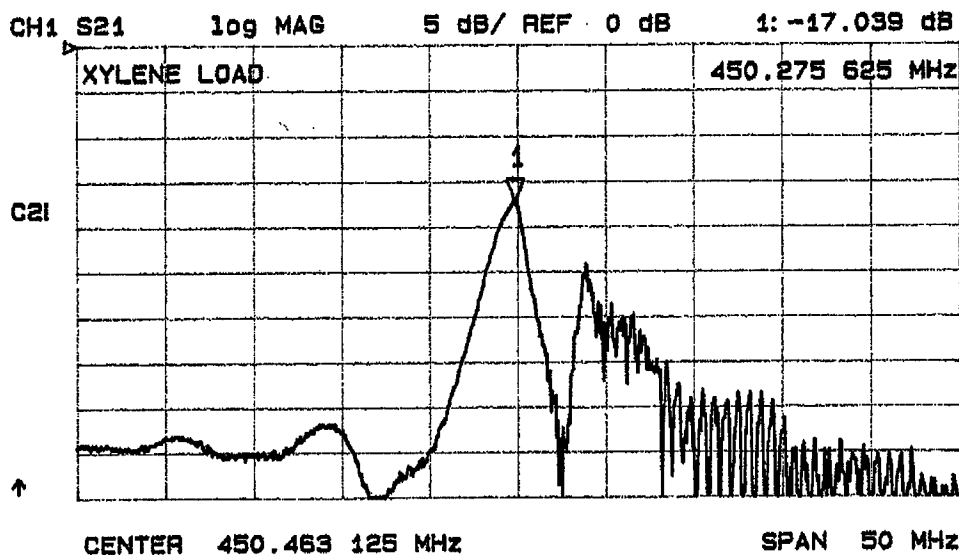


Figure 31. Xylene-loaded electrical response of the resonator with a 2,000 Å sputtered SiO₂ layer.

Structurally, BIODE has determined that resonators are preferable over delay lines and that high frequency resonators can be effectively designed. Liquid loading experiments indicate that the mass sensitivity of these STWs is a strong function of the silica thickness. The sensitivity of nominally 500 MHz STWs approaches a lower limit of $-20 \text{ ppm-mm}^2/\text{ng}$ sensitivity in the zero thickness limit and a maximum of $-120 \text{ ppm-mm}^2/\text{ng}$ at approximately a 5000Å silica film thickness. Obviously, these levels of sensitivity are desired. Given an approximate binding density of 0.1 ng/mm^2 , one expects a -12 ppm frequency shift from the optimized quartz STW. It is interesting to note that a 500 MHz TSM resonator would theoretically offer a sensitivity of $-140 \text{ ppm-mm}^2/\text{ng}$ if one could obtain the requisite 3-micron plate thickness. ***The measured mass sensitivity, as inferred from viscoelastic measurements, indicates that the 500 MHz STW approaches TSM sensitivity values, although it is generally accepted that surface waves cannot offer the same sensitivity as the TSM at a given frequency.***

Despite the progress in reducing the electrical loading effects on STW devices, none of the designs studied to date had sufficient insulation to operate as a biosensor with the entire active area loaded by the test liquid. The combined losses (viscous and capacitive) for 1μ films were $>14 \text{ dB}$ of additional losses for deionized water. Coupled with the losses due to internal friction of the polycrystalline films (3-5 dB) and the initial losses of 9 to 12 dB, the STW devices, to date, were unusable as biosensors.

During the next fiscal year, BIODE will determine whether the materials issues can be resolved. Resolution of these issues will allow BIODE to pursue sensors with picogram sensitivity limits. While the project schedule indicates that a decision would be reached at the end of FY1, BIODE proposes to amend this. SHAPM devices will be characterized as biosensors in FY2 while quartz and LTA STW devices are evaluated. BIODE will seek alternate funding to further pursue the STW effort, which will require substantial further effort. Were it not

for the 100 fold increases in sensitivity that could be accomplished, this effort would be discontinued.

II.B.6) Lithium Tantalate Surface Transverse Wave (STW)

BIODE has designed STW devices for lithium tantalate (36° RYC) which should operate at 420 MHz and are similar to the quartz STW currently in process. Initial lithium tantalate STW devices were patterned in March. Four wafers were processed through first level aluminum. One wafer was diced for preliminary electrical measurements prior to the addition of dielectric overlay. These devices behaved unexpectedly and provided unusable device responses. A corrected design provided slightly more comprehensible results. There appears to be a substantial difference between the electrical properties of SAW and STW devices on lithium tantalate, although SAW modeling has been reasonably useful on quartz. During the next quarter, BIODE will fabricate test wafers to evaluate the STW design properties. LTA STWs potentially overcome the electrical efficiency and dielectric loading issues of the quartz STW at the expense of temperature stability.

II.B.7) Quartz Monolithic Piezoelectric Sensor (MPS)

The monolithic piezoelectric sensor (MPS) is a dual monolithic resonator that has been mostly utilized in communications system filters. The MPS device is similar to the QCM device, but is a two-port device, which is more easily implemented as a feedback element in an oscillator. The MPS structure and its equivalent electrical circuit are shown in Figure 32.

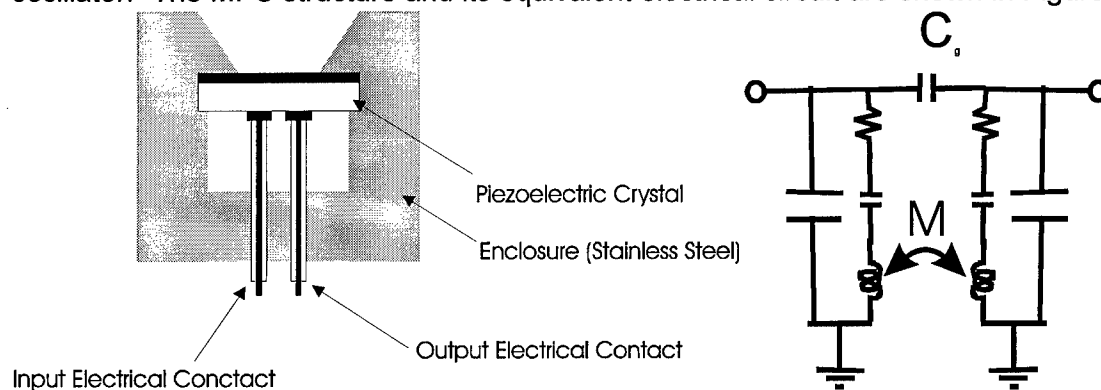


Figure 32. The MPS device packaged in a stainless steel enclosure (left) and its equivalent electrical circuit (right).

The first parameter considered for the design of the MPS was the type of piezoelectric material employed as the resonant structure. The MPS is to be used for sensing phenomena in fluids, so the acoustical standing wave must have shear-horizontal displacements, otherwise the acoustical energy will be dissipated into the fluid. This criterion limits the cuts of the piezoelectric materials that may be used. Another criterion for the MPS device is a desired insensitivity of the shear acoustic wave to changes in temperature. The AT cut of quartz (36° RYC) has a cubic shear-wave velocity response to temperature with an inflection temperature in the velocity-temperature spectrum at room temperature (approximately 24°C). This provides a temperature stable device when operated at room temperature and small changes (about 3°C) in temperature do not effect the operation frequency. Quartz also has a low intrinsic resistance so that the energy dissipation is small.

The next parameter to consider is the thickness of the piezoelectric material, which yields the resonant frequency of the MPS device. The thickness is the half-wavelength of the acoustic wave; therefore, the plate thickness is inversely proportional to the resonant frequency of the MPS. Since mass sensitivity is linearly proportional to operation frequency, the thickness

should be designed as thin as possible while maintaining durability for a fluid load. BLODE is currently modeling 50 MHz devices based on quartz "mesa" structures, but initial feasibility studies have been performed with 5 MHz devices since they were readily available [36].

The final parameter for the MPS design is the electrode design. BLODE has measured the electrical properties of first-pass and second-pass MPS sensors. These cut-and-try designs have provided the requisite insight for the development of design tools. In these tools, energy trapping analysis [37] was employed to ensure that the electrodes effectively trapped the fundamental symmetric and antisymmetric modes without trapping additional harmonic and anharmonic modes. A partial Mathcad® model of the structure has been constructed, which is also being applied to signal processing problems in cooperation with a quartz crystal vendor. While it predicts the resonant frequencies and fixture losses, it cannot predict the other electrical properties of the device and is extremely slow. Eagleware SuperStar Pro® has been employed to further model the sensor. National Science Foundation (NSF) funding has been requested to fund the development of a device model based on coupling of modes (COM) theory and numerical solution to the wave equations and boundary problems in the various media.

The electrode design consists of the geometry, area and metal thickness of the electrodes combined with the gap width between the electrodes. A graphical representation of the energy trapping due to the electrodes is shown in Figure 33. The geometry of the electrodes is rectangular for easy mathematical modeling. The electrode area, which traps the symmetric and antisymmetric modes, has a width of 7 mm, a length of 11 mm and a gap width of 3 mm. The electrode thickness is 150 nm of aluminum for this electrode geometry. This most recent design is currently being manufactured and will be tested in FY2, Q1.

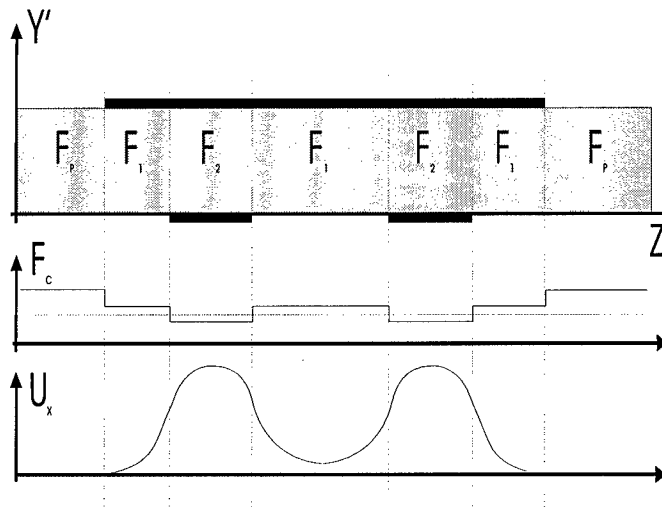


Figure 33. The waveguide cross-section (upper) consists of seven regions with cutoff frequencies F_p (piezoelectric), $F_1 = F_p - \Delta F_1$ (single electrode) and $F_2 = F_p - \Delta F_1 - \Delta F_2 - \Delta F_p$. The relative cutoff frequencies are shown (center) along with a frequency solving the boundary conditions (dashed line). A typical amplitude profile is shown for a symmetric mode (lower). The mode is trapped to the regions of paired electrodes and decays exponentially outside these regions.

A second-pass design has been evaluated for frequency shifts and Q degradation under viscous liquid loading. When a viscoelastic liquid loads one side of the sensor, both the shape and the center frequency of the resonance are altered. Figure 34 provides theoretical responses for air, deionized water and three glycerin solutions (43%, 64% and 80%) in water. The separation between the symmetric and antisymmetric resonances increases although the mutual inductance is unchanged. The center frequency changes about half as rapidly as the separation between the resonances. The net effect is that the antisymmetric resonance is

essentially unchanged by viscous liquid loading while the symmetric resonance is extremely sensitive to this perturbation.

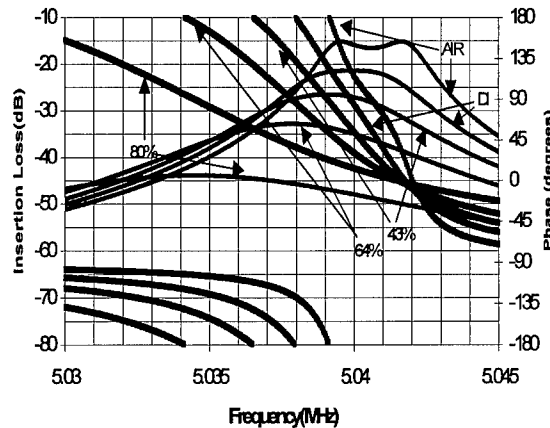


Figure 34. Theoretical response of the prototype device to various viscous liquids.

Experimental data for these liquids are given in Figure 35. Excellent agreement is observed. Even at 80% glycerin, theory and experiment agree to within a few dB.

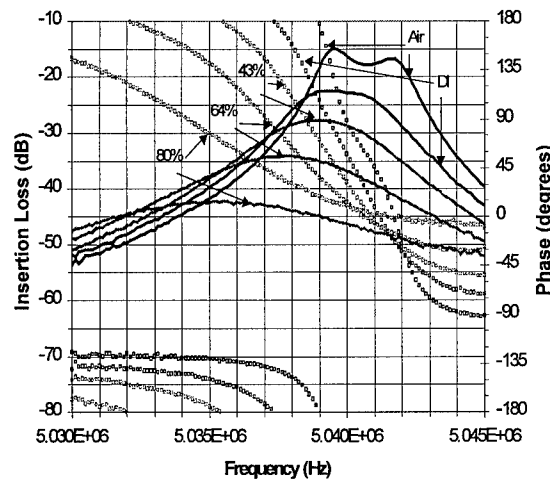


Figure 35. Experimental electrical characteristics (S_{21}) of the MPS prototype with viscous fluid loading. Agreement with theory is excellent. Perturbations by viscous liquids are distinguishable from perturbations due to rigid solid films.

Further design and modeling efforts have been promising. The MPS provided excellent agreement between theory and experiment for viscous liquids. The predicted mass sensitivity is $-1.4 \text{ ppm-mm}^2/\text{ng}$ at 5 MHz and increases linearly with increasing frequency. This value is supported by the aforementioned viscous loading measurements.

The MPS appears to be a very promising method of detecting subnanogram quantities of measurands. The evaluation of the MPS sensitivity and stability need to be performed with oscillator based measurements. Currently, all data have been taken using impedance spectroscopy techniques. This method yields information on the MPS, itself, and the effect of the surface and liquid chemical interactions. The incorporation of the MPS into a stable, low-noise oscillator circuit does not appear to be difficult, once the MPS is designed to have the appropriate electrical characteristics.

II.C) Measurement Electronics

II.C.1) Scope and Schedule. Extensions to Scope.

BIODE has performed research on both oscillator and phase bridge techniques. Oscillator design is complete to the degree specified in the contract. *Discussions with other researchers have underlined the need to add automatic gain control to the system in order to decrease noise processes.* Phase bridge research is slightly behind schedule; partially since additional methods are being investigated. Simple systems, based on diode ring mixers, have been tested but require excessive signal power. Active (transistor) mixers are being investigated and appear promising – especially in terms of the potential for integration into a single monolithic microwave integrated circuit (MMIC) containing all of the high frequency electronics for a sensor and reference pair.

II.C.2) Oscillator Electronics

We have explored the Hewlett Packard INA12063 chip amplifiers in comparison to the Minicircuits MAR-6SM for use in the oscillators. As stated in previous reports, the INA consumes between 5 and 10 mA and is extremely small. The MAR consumes 16 mA and is considerably larger. A recent improvement on the MAR is the VAM series, which has the same electrical performance as the MAR but is the same size as the INA. Thus, board area is no longer a consideration between these two techniques. Preliminary efforts indicated that the INA was unsuitable as an oscillator. We found that the addition of a 330Ω in the bias network eliminated a 1.5 MHz oscillation, which precluded proper operation. Small size is critical if four oscillators are to be employed to instrument four sensors in a single package.

BIODE has received commercially manufactured dual and quad oscillator prototypes, which were subsequently evaluated. Power consumption is currently 20mA at 3.3V per oscillator, including the buffer amplifiers. Since the 3.3V signals are independently regulated from a common 5V source, the total power consumption is 100mW per oscillator. Lower power oscillators have been tested and worked well in isolation; however, multiple oscillators are subject to high levels of mutual electromagnetic interference. To overcome this, higher bias levels are required. Sequential operation of the oscillators will provide total elimination of inter-oscillator cross-talk and still provide data often enough for analysis. Automatic gain control (AGC) circuitry can help limit this effect while allowing simultaneous measurements.

Results of stability tests on multiple oscillators indicate a potential problem with the SHAPM, most notably the YX-LTA devices, wherein strong phase noise sources are associated with the adjacent acoustic modes. These noise sources can be described as "almost" oscillators. The net gain around the loop is not quite unity; however, external noise and nonlinear translation of energy from the main resonance pump energy into the circuit at the noise frequency. The result is a high level of noise at specific frequencies. In terms of the time stability, this leads to a chaotic frequency modulation, which can mask true sensor responses. Oscillator applications favor the MPS and STW sensors.

II.C.3) Phase Interferometry

BIODE has begun prototyping phase bridge techniques that may overcome the issues of high insertion loss that limit the applicability of quartz STW sensors and current MPS sensors. Additionally, phase bridge techniques are less susceptible to electromagnetic interference and alleviate injection locking, which occurs between closely placed oscillators. Functional blocks have been prototyped and have provided encouraging results. Additional prototypes will be manufactured and evaluated.

In order to allow a high degree of integration, active (transistor) mixers, such as the IAM-81008 from Hewlett-Packard were considered. Four sets of experiments were run using the

IAM active double balanced mixer. A resistor network was placed in the signal path between the in-phase output of the power splitter and the RF input of the IAM. Tests were performed using no resistive pad (0 dB) and resistor π networks to simulate -5dB , -10dB , -15dB losses. These various resistor networks produced RF signals of -5dB , -10dB , -15dB and -20dB , respectively. An input signal into the power splitter of -2 dBm , combined with the power splitter's -3dB of loss to each output, provided the additional -5dB of the RF signal. Using the same arrangement, the LO signal into the IAM was kept at a constant -5dB throughout the experiments. The output voltage was measured for various lengths of cable ranging from 0 to 120 cm in 15 cm increments for each resistor network. Plotting the output voltage vs. the phase inherent in each length of cable produced the theoretically expected behavior, in which voltage is proportional to the cosine of the phase plus a constant bias value. As the loss in the resistor network decreased, the peak amplitude of the phase-induced voltage increased, as seen in *Figure 36*. Higher RF drive levels provide enhanced sensitivity.

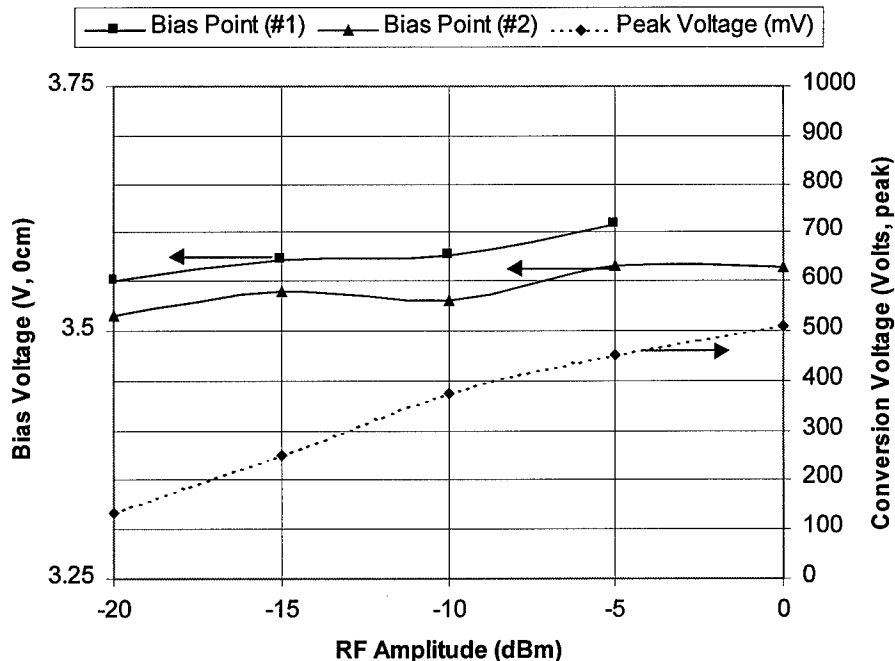


Figure 36. Bias Voltage (left) at quadrature and peak conversion voltage (1/2 of difference between 0° and 180° values) for IAM 81008 active mixer. LO power was -5 dBm throughout.

The reproducibility of the output voltage at quadrature phase (bias value) is important, since it is the reference value against which phase is measured. Bias points are indicated for two different mixers in *Figure 36* over a range of RF power levels. The behavior of the two mixers to variations in RF power is comparable. The figure shows approximately 35 mV of offset between the two devices, which corresponds to approximately 10° of absolute phase error. Absolute phase error on the order of 10° is not critical to the application, which requires knowledge only of small phase changes. Reproducibility over changes in RF power are important. The responses are reproducibly nonlinear; however, additional samples must be measured to obtain statistically significant data.

A more critical parameter is the effect of ambient temperature on the mixer's bias point, shown in *Figure 37*. Measurements indicate a linear dependence of the voltage with temperature (0.7 to $0.8\text{ mV}/^\circ\text{C}$), which represents approximately a 0.1° phase error per $^\circ\text{C}$ at high drive levels. For the device with the lowest total phase shift ($14,400^\circ$ for the 63 MHz LTA SHAPM) and the highest RF drive levels, this corresponds to $7.5\text{ ppm}/^\circ\text{C}$. Since correction for

device temperature is already under consideration, correcting for mixer (ambient) temperature is not a substantial additional problem. Further effort on the phase bridge will continue into FY2.

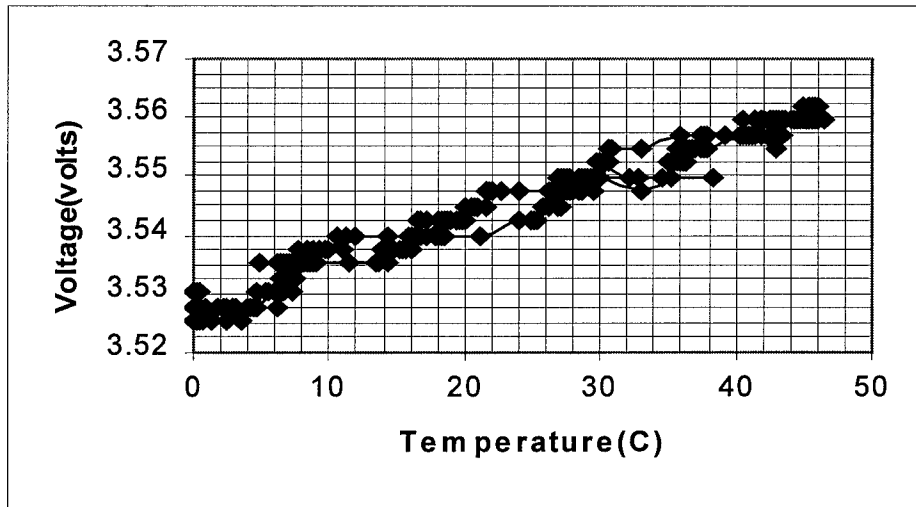


Figure 37. Temperature stability of the bias point for -5 dBm LO and 0 dBm RF drive levels. The slope is approximately 7.5 mV/ $^{\circ}$ C, which corresponds to only 1° phase per $^{\circ}$ C near quadrature.

II.C.4) Support Electronics (Frequency Counters, Frequency Prescalers, Temperature Measurement and Electrochemical Control)

In support of the oscillator technique, BIODE has devised novel electronic counting circuitry based on in-phase / quadrature demodulation technology and digital aliasing mixers. We have designed and manufactured single channel (sensor + reference) boards using a mixture of Fairchild Advanced Schottkey Technology (FAST) and low voltage CMOS technology. These boards provide a model of a pending integrated circuit design, allowing microcontroller programming and testing to occur while the IC is designed and manufactured. The circuit boards are capable of approximately counting the difference frequency between two signals with individual frequencies up to 120 MHz and are capable of counting individual frequencies to about 200 MHz. *We have initiated a custom IC implementation of the circuit, under alternate funding.* These circuits will miniaturize the electronics required for four sensors and a reference when employed with oscillator based electronics. The subcontractor is attempting to implement the oscillator electronics on-chip as well, offering substantial miniaturization potential beyond the integration of the digital functions.

Frequency prescalers have been designed and tested to implement divide-by-2, -4, or -8 frequency reduction. Thus, even a 1.2 GHz STW sensor could be instrumented with the temporary frequency counter boards using divide-by-8 prescaling.

Lithium tantalate and, to a lesser degree, quartz devices require residual temperature correction. In order to obtain ± 0.1 ppm absolute resolution of frequency shifts with lithium tantalate, it is necessary to measure temperature to approximately 0.01° C resolution. Note that absolute temperature need not be known. Only changes in temperature must be resolved. Work on this requirement is in progress. Resistive and thermocouple techniques have been evaluated and have provided 0.1° C resolution. One approach that has been suggested in the literature is to employ a SAW oscillator with a high temperature coefficient of frequency (TCF) as a thermometer. The SAW would not interact with the sensing surface and would ideally only respond to temperature changes. It is conceivable that such a sensor could be instrumented using one of the four channels of the frequency counter. The primary obstacle is placing the SAW thermometer in close contact with the sensing device. One approach is to employ the

SAW propagating in the Z direction on a Y-cut lithium tantalate wafer, which has a TCF of ~33 ppm/°C. A resolution of 0.1 ppm would result in temperature change resolutions of approximately 0.003°C. A similar approach uses an STW propagating at 90° from the SHAPM on -65°RYC quartz. In these cases, the SAW would exist on the same chip as the SHAPM and would be completely encapsulated from the liquid.

Finally, electrochemical circuitry has been developed under parallel research (DE-FG02-94ER-81717). This circuitry may be applicable to the current effort, should electrochemical reversal of antibody-antigen reactions prove feasible. The electrochemical board has four electrochemical circuits, one for each device, and a header that will interface to a DAC and ADC on the microcontroller or data acquisition system. The DAC circuitry will apply a requested electrochemical potential. The circuit compensates resistive drops and counter electrode surface potential by placing a reference electrode (e.g. silver/silver chloride) into the feedback path. The ADC circuitry monitors the electrode current into the device surface.

II.D) Packaging and User Interface

II.D.1) Introduction.

An acoustic plate mode (APM) sensor controller prototype is been developed that will be capable of performing operations pertaining to information gathering, processing, and distribution as well as waveform generation which can be used for sensor electrochemistry. The platform can take sensor data in the form of frequencies, analog voltages, or digital signals with several signals presently defined and implemented. The data can be corrected for temperature or other factors with predefined algorithms, and can be displayed to an LCD or sent to an external PC via an RS-232 port, whose interface protocol is under development. In the future, the platform will be capable of interfacing to the E-SMART network, an environmental sensor standard, and to the IEEE general purpose interface bus (GPIB).

II.D.2) Microcontroller

The controller consists of a microprocessor chip with a built in analog to digital converter (ADC), a differential frequency counter (DFC), a digital to analog converter (DAC), a liquid crystal display (LCD), a keypad and encoder chip, and a power supply. The microprocessor used for the prototype controller is a Motorola MC68HC916X1 chip. The network consists of some form of transmission media, hardware to interface with the controller, and a communication protocol. Currently, communications is limited to RS-232 interface between the controller and a host.

The efforts to date will be discussed in five different subsections, one subsection devoted to each module. The main system comprises the HC916 chip, the evaluation board, and O/S (operating system) code. The LCD (liquid crystal display) section will discuss the LCD code and display screen. The keypad section discusses the code and hardware, as well as the use of a keypad decoder chip. Following will be a brief electrochemical waveform code description and a summary of the DAC (digital-to-analog converter) that was used. Effort to date on the serial interface and protocol will be discussed, as well as the RS-232 cable/interface. Concluding the results section will be a short description of the frequency processing code and DFC (differential frequency counter) interface.

II.D.2.a) Main system overview and code/system information

The chip that was purchased to serve as the heart of the system was Motorola's MC68HC916X1 [38,39]. This is a new 16-bit chip from Motorola with a number of features, including multiple input event capture and output event capabilities, 2 pulse-width modulators

(PWM), a periodic interrupt timer (PIT) and a watchdog timer. The chip supports background debugger mode (BDM) for development or debugging and a single-chip mode.

There is 50K of Electrically-Erasable Programmable Read Only Memory (EEPROM) and 2K of static RAM (Random Access Memory). The HC916 runs at 5V with a maximum clock speed of 16.78 MHz. It has a built-in Analog-Digital Converter (ADC), Serial Communication Interface Module (SCIM), and a General Purpose Timer (GPT). The chip has a very small footprint (120-lead Thin Quad Flat Pack (TQFP)), measuring 0.5mm x 16mm x 16mm, yet still has 95 possible input/output (I/O) lines.

Because a C compiler [40] was used, the code was written in a traditional function-oriented design paradigm. Upon power-up or reset, a startup routine is called that will initialize the chip's memory, code locations, etc. This function exits and the main function is called. This function contains or calls all of the user code.

The operating system (O/S) calls a platform initialization routine, which initializes all of the different modules. It then prints a message to the screen telling the user that they must press the "enter" key after they enter data or a command. Next, a series of decision screen are presented which will determine which functions the users wants to use. After the user has selected a function, the program will execute that module and return upon completion.

II.D.2.b) Liquid crystal display (LCD) overview

An LCD was purchased to facilitate microprocessor-user communication. The LCD is used to display information to the operator. The LCD has 4 rows and 40 columns (Optrex DMC-40457 dot matrix LCD module) [41]. The LCD interfaces to the microcontroller via an 8 bit parallel interface with read-write (R/W), row select (RS) and two bank enable (E1 and E2) control lines, which regulate the passage of data and other LCD operations.

The E1 line enables the first two lines of the LCD (bank 1) and the E2 line enables the third and fourth lines (bank 2). The LCD has numerous features such as a clear display function, cursor at home (returns a cursor to the starting row and column), enable or disable cursor presence or blinking. The LCD can also shift the cursor as well as the display.

A library of functions has been written to enable the use of the LCD. Functions exist to make use of the LCD pre-defined operations. A user function has been written that will print a string or strings to the screen. More specific functions have been written that implement the menu interfaces for each module.

II.D.2.c) Keypad/encoder overview

A keypad is used to take commands and data from the user. The keypad purchased was a series-86, 20-key Grayhill keyboard [42]. This keyboard has such features as ½" button centers and a snap-dome contact to provide positive feedback. The keypad encoder that was purchased was a MM74C923 20-key encoder from National Semiconductor [43]. The encoder provided a 50 kΩ maximum switch resistance, 2-key roll-over and bounce elimination. It requires a single external capacitor, and exhibits low power consumption.

A circular data buffer is used to store the information received from the keypad. Specific routines have been written to read and write data in the buffer and to process the key strokes. Since the keypad encoder is designed for a 5x4 keypad rather than a 4x5 keypad, the data received from the encoder must be corrected through the use of a look up table. A data structure containing control bits is used to handle keypad control by locking/unlocking the keypad, echoing/not echoing keys, etc.

II.D.2.d) Waveform/digital-analog converter overview

The electrochemical waveform generator was developed under parallel funding (DE-FG02-94ER-81717) and is reported here since electrochemical stripping of toxins from antibody

is contemplated. A serial DAC is to convert digital numbers to electrical potentials between $-2.5V$ and $2.5V$. These values control the electrochemistry board, discussed earlier. The existing waveform function can generate anything from a square wave to a triangle wave, by varying the parameters of the typical waveform in Figure 38. The DAC is a low-cost, 8-bit CMOS, 8-output DAC which uses a 3-line serial interface to communicate with the MCU.

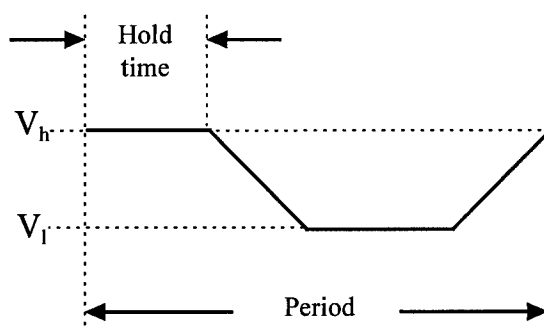


Figure 38. Sample electrochemical waveform

The existing function supports an Analog Devices DAC8800 8-bit CMOS DAC [4] connected to pins PGP[5:7] of the HC916X1 processor. The processor uses pin GP5 for the chip clock, GP6 for the serial data interface (SDI), and GP7 for the LD data line.

Code exists to gather the voltage parameters from the user and check them for validity. Two routines handle initializing and writing the waveform, and one is used to terminate it.

II.D.2.e) Serial communication overview

Serial communication refers to the transmission of data over a single line with several other lines used to control the transmission of data. This is a desirable method to interface the MCU with an external PC for a variety of reasons. The foremost design motivation is the ability to download sensor data from the platform to the PC, but other possibilities are upgrading sensor firmware, debugging possible problems on a platform, or downloading calibration data from the PC to the MCU.

This interface will be accomplished using a 25-pin RS-232 cable connected to the 25-pin RS-232 port on the MPFB1632 board (the HC916 evaluation board). The main operating code will ask the user whether they want local or external control. If they select external control then the system will initialize the serial port and wait for commands from the PC. When a valid string is received, the HC916 will carry out the corresponding operation.

II.D.2.f) Differential frequency counter (DFC) overview

The differential frequency counter (DFC) was described earlier. It accumulates zero crossings from four external signal sources, either as raw frequencies or as frequency offset from a reference signal. These 32-bit values are read in a byte-by-byte fashion from the counter. The data is merged other information such as temperature and operated on by algorithms to determine the amount of measurand. The algorithms have not yet been devised. The DFC system consists of four counters.

Aside from an initialization routine, there is currently only one other function used for this module. This function reads either the raw or differential frequencies as specified. The routine uses a 2 second sample period and divides the result by two. This is done because the DFC board is designed for a user-defined gate period and 2 seconds is accurately obtained as 125 periods of the PIT using a 16 MHz system clock. An arbitrary gate period would require a floating-point division to obtain the frequency. However, a 2-second gate allows a simple binary shift.

II.E) Characterize the Phase II Prototypes (data from DAAM01-95C-0076)

An MUA SAM was used to provide a -COOH surface. EDC-mediated attachment of rabbit anti-goat IgG was employed as a control surface (Jackson Immuno Research). EDC-mediated attachment of rabbit anti Y. Pestis IgG was employed to activate the sensor surface (A1122 LEADERLE, lot C11214A, USAMRIID). The dual sensor was incorporated into a battery powered oscillator (>6VDC@100 mA). Measurement of oscillator outputs was performed using a laboratory frequency counter and PC.

Y. Pestis killed cells of unknown initial concentration were diluted in successive 10:1 ratios. We assume a 500 µg/µl (500 mg/ml) maximum possible concentration prior to dilution and 5 µg/µl (5 mg/ml) minimum possible concentration of Y. Pestis. Seven 10:1 dilutions (down to 0.5 pg/µl to 50 pg/µl range) were performed. Goat IgG is stock at 5 µg/µl. Five 10:1 dilutions (down to 50 pg/µl) were performed.

A static sample was evaluated. Additions of 5 µl into a nominally 600µl static fluid cell approximate a 100:1 secondary dilution. Added quantities will be on the order of 250 pg or less at the lowest concentration. First, Y. Pestis was added and the associated frequency shift was measured. After all additions of Y. Pestis, Rabbit IgG was added and the alternate sensor frequency shift was measured.

Measurements were performed for Y. Pestis dilutions of 10^{-5} , 10^{-4} and 10^{-3} from killed cell solution (lot #1151, 1-26-96, A1122, irradiated 9.6×10^9 J). No response was observed to a 5 µl addition of the 10^{-5} dilution. A -0.25 ppm shift was observed for a 5 µl addition of the 10^{-4} dilution and a saturated response (-0.5 ppm total) was observed for a 5 µl addition of the 10^{-3} dilution. These additions correspond to final solution concentrations between 10^{-7} and 10^{-5} of the unknown stock solution.

Following saturation of the Y. Pestis sensing channel, calibration with known quantities of goat IgG was performed. An addition of 5 µl of 5 ng/µl goat IgG was added and resulted in a slow response of -0.5 ppm (+/- 0.1 ppm). The agreement with the saturated response of the Y. Pestis channel is encouraging.

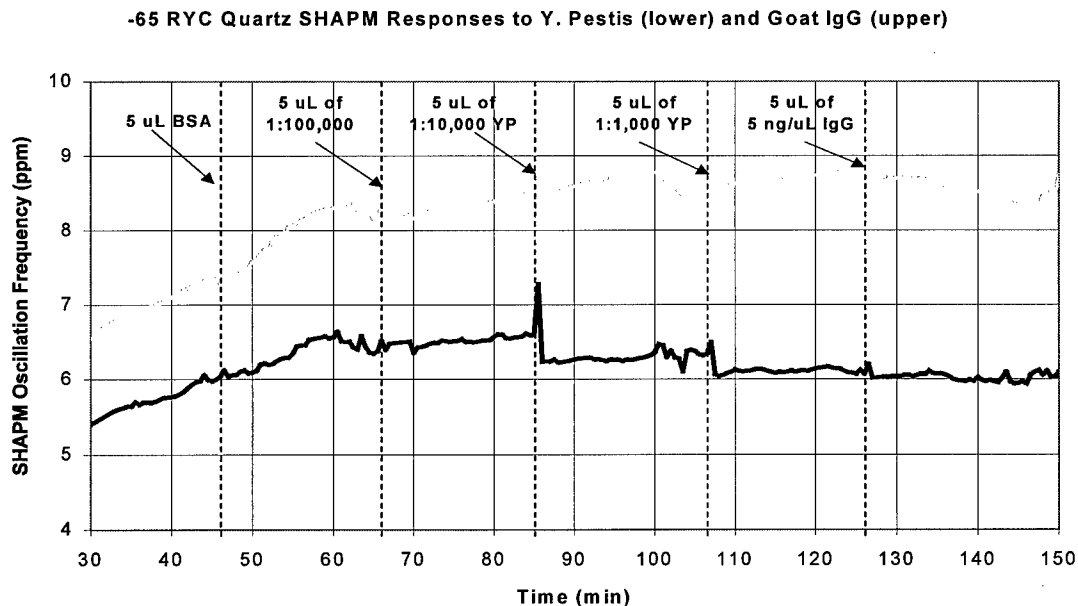


Figure 39. Response of the -65° RYC quartz SHAPM to Y. Pestis cellular proteins (sensor device antibody, lower trace) and Goat IgG (reference device antibody, upper trace). Measurable responses are observed; however, further improvement is needed.

II.F) Project Status for FY1 and Recommended Research and Development for FY2

II.F.1) Current Status of Attachment Chemistry

PMS has demonstrated good reproducibility, low cross-reactivity and excellent longevity. The fundamental objections to PMS are the author's mistrust of exposed disulfide bonds and the requirement to thioalkylate the antibody prior to attachment. Thiodialkynes have exhibited excellent properties; however, they possess very short shelf lives, are difficult to synthesize and are not commercially available. Since the binding densities are comparable, PMS will be employed as the primary attachment chemical in biosensor testing while reliability and screening tests are performed on thiodialkyne and thioalkene processes. Remaining work on the attachment chemistry is as follows:

II.F.1.a) Perform electrochemical tests on PMS films with $\text{Fe}(\text{CN})_6^{-3}$.

The quality control tests studied for thioalkane and thiodialkyne films should be repeated for PMS-based attachment processes. The ability to verify production scale manufacture of biosensors is important and could be a deciding factor in the final selected chemistry.

II.F.1.b) Continue longevity tests.

Ongoing PMS longevity (storage) tests should be continued through the end of the project. Similar tests on thiodialkyne and thioalkene processes should be initiated.

II.F.1.c) Perform thiodialkyne longevity / regeneration test.

Longevity tests and regeneration tests, which were performed on PMS, should be repeated on thiodialkyne films.

II.F.1.d) Perform initial study of thioalkene process.

A new process combines the cross-linking features of the thiodialkyne process and the shelf-life of PMS. The process employs 11-mercaptoundecene, $\text{HS}(\text{CH}_2)_9\text{CH}=\text{CH}_2$, as a SAM film. Peroxides are employed to convert the double bond to a terminal epoxide. Exposure to glycine incorporates carboxyl functionals to some of the epoxides. These opened epoxides combine with adjacent epoxides, forming a cross-linked polyethylene oxide surface. The new technique requires substantial development and current funds will only be employed to determine feasibility.

II.F.1.e) Perform initial study of electrochemical biochemistry.

Two opportunities exist relative to applying biochemistry to the biosensor. First, virtually all attachment processes that BIODÉ has studied have a limiting surface capacity of $<1 \text{ ng/mm}^2$, while the theoretical limit is approximately 10 ng/mm^2 without accounting for surface roughness. One explanation is that the attachment of charged biochemicals leads to the accumulation of a retarding charge that limits the process. The effects of electrochemical bias during antibody attachment should be determined.

Second, covalently bound antibody should survive mild electrochemical cycling; however, these cycles should alter the ionic binding between antibody and toxin, releasing bound toxins under the appropriate bias. These techniques would also require substantial development and current funds would only be employed to determine feasibility.

II.F.2) Status and Recommendations for the Piezoelectric Sensor

The SHAPM is the most mature technology of the three proposed. Both LTA and quartz SHAPM devices will be compared in biochemical testing. The MPS offers the same sensitivity

at lower operating frequencies and offers the potential for 10-fold sensitivity improvement based on preliminary device models. The STW presents the most risk and, not surprisingly, the most potential for performance increase. Both the MPS and the STW will be pursued, on a time permitting basis. Should substantial progress be made in either device, testing will compare the best SHAPM device with the new technology. Specific tasks to be performed under FY2 effort include:

II.F.2.a) SHAPM Devices

Both the quartz and lithium tantalate SHAPM offer the possibility of placing a surface wave thermometer on the electroded surface of the sensor. This would allow extremely high resolution measurement of temperature changes and would allow precise temperature correction of small offsets in a self-calibrated system. Resonator structures are being designed for the quartz material. Pending successes with quartz resonators, lithium tantalate resonators will be considered. After further consideration of the YX lithium tantalate devices, the use of orientations between 10° and 20° RYC lithium tantalate will be considered. These orientations offer at least a two-fold reduction in temperature sensitivity at the expense of a decrease in mass sensitivity.

II.F.2.b) STW Devices

Further evaluation of STW device feasibility is planned; however, the development effort required to successfully capitalize on the 100-fold increase in mass sensitivity appear to exceed the remaining scope of this contract. Alternate funding for this effort should be sought with current effort focussing on SHAPM and instrumentation. Once developed, STW technology could be employed to upgrade the instrument with minor changes to the other functional systems. Limited research on STW devices will be performed in order to obtain supporting data for future research.

II.F.2.c) MPS Devices

Again, additional effort is required on the MPS devices. FY2 effort in Q1 will determine the applicability of the MPS to the immediate application. MPS technology is expected to offer a 3 to 10-fold improvement in sensitivity and could be developed during the course of the current effort.

II.F.3) Status of the Measurement Electronics

In order for the phase method to succeed, it must resolve phase changes to better than 0.1 ppm of the nominal phase ($\omega\tau$) of the device. An upper limit for SHAPM delay lines is between 36,000 and 72,000°, requiring a detection limit of 0.0036° to 0.0072°. At 500 mV peak voltage from the mixer, the required voltage sensitivity is, at best, 63 μ V ($500\pi/180$ mV/° times 0.0072°) at quadrature and less at nominal phase values away from quadrature. Thus, the data acquisition system must reliably amplify and detect 30 to 60 μ V signals. Resonator structures exhibit higher frequency-delay products (approximately 10-fold), requiring sensitivity limits on the order of 0.5mV. These levels are below the noise performance of discrete systems; however, on-chip signals in an integrated circuit could achieve these levels.

Oscillators operating in proximity are currently problematic. Careful design has overcome this problem in many cases. The addition of automatic gain control (AGC) should overcome this problem in most cases. In the limited cases where problems still exist, sequential operation of the oscillators is an option.

Another option overcomes the limitations of both multiple oscillators and the phase interferometer. One device (the reference) is employed to stabilize a voltage controlled oscillator (VCO). The VCO output drives the other device (sensor) and the phase detector. The

resulting voltage is fed back to the VCO and adjusts the operating frequency. Common changes in the reference and sensor compensate and either the VCO frequency or the phase detector voltage may be employed to instrument the system. FY2 effort will complete the study of phase interferometry, incorporate AGC and VCO capabilities into the oscillators and evaluate the phase-locked oscillator (PLO) concept, discussed above. This technique appears to be robust and sensitive.

II.F.4) Status of the Microcontroller

The most substantial tasks remaining for the microcontroller are systems integration and the development of sensor calibration and data extraction algorithms.

II.F.5) Biosensor Measurements

These measurements represent the majority of the FY2 effort, especially in Q2-Q4.

III) References

1. J. C. Andle and J. F. Vetelino, "Acoustic Wave-Based Biosensors", Invited paper, *Sensors and Actuators A*, v 44-3, pp. 167-176 (1994).
2. R. Dahint, M. Grunze, F. Josse and J. C. Andle, "Probing of Strong and Weak Electrolytes with Acoustic Wave Fields", *Sens. & Act. B* 9, 2, pp. 113-120 (1992).
3. S. J. Martin, A. J. Ricco, T. M. Niemczyk and G. C. Frye, "Characterization of SH Acoustic Plate Mode Liquid Sensors", *Sens. & Act. B* 20, 253-268, (1989) and ref. therein.
4. J. C. Andle and J. F. Vetelino, "Acoustic Wave-Based Biosensors", Invited paper, *Sensors and Actuators A*, v 44-3, pp. 167-176 (1994).
5. J.C. Andle, D. J. McAllister and J. F. Vetelino, "Shear Horizontal Acoustic Plate Mode Sensors for Biochemical Detection", *Scientific Conf. on Chem. and Bio. Defense Research*, pp. 617-623, (1994).
- 6 Private Communications. Dr. Frank Smith, King's College.
7. C. Kosslinger, E. Uttenthaler, S. Drost, F. Aberl, H. Wolf, G. Brink, A. Stanglmaier and E. Sackmann, "Comparison Of The QCM And The SPR Method For Surface Studies And Immunological Applications", *Sensors and Actuators B*: 24-25 (1995) 107-112.
8. S. Martin, V. Granstaff and G. Frye, "Characterization of a Quartz Crystal Microbalance with Simultaneous Mass and Liquid Loading", *Anal Chem* 1991, 63, 2272-2281.
9. Private discussions with Steve Martin, Tony Ricco and Ross Thomas, Sandia National Labs, Albuquerque, NM. Feb., 1996.
10. M. Rodahl, F. Hook and B. Kasemo, "QCM Operation in Liquids: An Explanation of Measured Variations in Frequency and Q Factor with Liquid Conductivity", *Anal Chem* 1996, 68, 2219-2227.
11. T. Schneider and S. Martin, "Influence of Compressional Wave Generation on Thickness-Shear Mode Resonator Response in a Fluid", *Anal Chem* 1995, 67, 3324-3335.
12. L. Tessler, F. Patat, N. Schmitt, G. Feuillard and M. Thompson, "Effect of the Generation of Compressional Waves on the Response of Thickness-Shear Mode Acoustic Wave Sensors in Liquids", *Anal Chem* 1994, 66, 3569-3574.
13. H.T. Sun, M. Faccio, C. Cantalini and M. Pelino, "Impedance Analysis and Circuit Simulation of Quartz Resonator in Water at Different Temperatures", *Sensors and Actuators B* 32 (1996) 169-173.
14. M. Noel and P. Topart, "High Frequency Impedance Analysis of Quartz Crystal Microbalances. 1. General Considerations", *Anal Chem* 1994 66, 484-491.

-
15. H. Su, M. Yang, K. Kallury and M. Thompson, "Network Analysis: Acoustic Energy Transmission Detection of Polynucleotide Hybridization at the Sensor-Liquid Interface", *Analyst* 118, March, 1993, 309-312.
 16. S. Bruckenstein, M. Michalski, A. Fensmore, Z. Li and A. Hillman, "Dual Quartz Microbalance Oscillator Circuit. Minimizing Effects due to Liquid Viscosity, Density and Temperature", *Anal Chem* 1994, 66, 1847-1852.
 17. G. Dunham, N. Benson, D. Petelenz and J. Janata, "Dual Quartz Crystal Microbalance", *Anal Chem* 1995, 67, 267-272.
 18. S. J. Martin, A. J. Ricco, T. M. Niemczyk and G. C. Frye, "Characterization of SH Acoustic Plate Mode Liquid Sensors", *Sensors and Actuators*, 20, pp. 253-268 (1989).
 19. J. C. Andle, J. F. Vetelino, M. W. Lade and D. J. McAllister, "An Acoustic Plate Mode Biosensor", *Sensors and Actuators B* 8, 191-198 (1992).
 20. J. C. Andle, J. T. Weaver, D. J. McAllister, F. Josse and J. F. Vetelino, "An Improved Acoustic Plate Mode Biosensor", *Sensors & Actuators B* 13, n. 1-3, 437-442 (1993).
 21. J. Andle, J. Weaver, J. Vetelino and D. McAllister, "Selective Acoustic Plate Mode DNA Sensor", 5th Int'l Meeting on Chemical Sensors, July, 1994, Rome, Italy, pp. 152-155.
 22. F. Josse, J. Andle, J. Vetelino, R. Dahint and M. Grunze, "Theoretical and Experimental Study of Mass Sensitivity of PSAW-APMs on ZX-LiNbO₃", *IEEE Trans. on Ultrasonics, Ferroelectrics and Frequency Control*, Vol. 43, No. 4, pp. 517-524, July 1995.
 23. J. C. Andle, An Experimental and Theoretical Analysis of Acoustic Plate Mode Devices for Biosensor Applications, Ph.D. Dissertation, University of Maine (1993)
 24. J. C. Andle, M. G. Schweyer and J. F. Vetelino, "Acoustic Plate Mode Properties of Rotated Y-Cut Quartz", 1996 Frequency Control Symposium, pp. 532-540 (1996).
 25. J. C. Andle, M. G. Schweyer, L. A. French and J. F. Vetelino, "Experimental Acoustic Plate Mode Properties of Rotated Y-Cut Quartz", 1996 IEEE UFFC Symp., pp. 532-540 (1996).
 26. F. Josse, Design, Fabrication and Testing of Surface Skimming Bulk Wave Devices, MS Thesis (1979) & Analysis of the Generation, Interaction and Detection of Surface and Bulk Acoustic Waves on Piezoelectric Substrates, Ph.D. Thesis, University of Maine (1982).
 27. Z. Shana and F. Josse, "Analysis of Liquid Phase Based Sensors Utilizing SH-Surface Acoustic Waves on Rotated Y-Quartz", *Proc. of the 1988 IEEE Symp. on UFFC*, 549-554.
 28. E. Gizeli, N. Goddard and C. Lowe, "A Love Plate Biosensor Utilizing a Polymer Layer", *Sensors & Actuators B*, 6 (1992) 131-137.
 29. G. Kovacs, G. Lubking, M. Vellekoop and A. Venema, "Love Waves for Biochemical Sensing in Liquids", *Proc. of the 1992 IEEE Symp. on UFFC*, 281-285.
 30. R.L. Baer, C.A. Flory, M. Tom-Moy and D.S. Solomon, "STW Chemical Sensors", *Proc. 1992 Ultrasonics Symp.*, pp. 293-298 (1991).
 31. C. Flory and R. Baer, "STW Mode Analysis and Coupling to IDTs", 1987 Ultrason. Symp., 313-318.
 32. J. Height, D. Huynh, J. Weaver, M. Schweyer, J. Andle, D. McAllister and J. Vetelino, "Comparison Of Surface Transverse Wave (STW) And Shear Horizontal Acoustic Plate Mode (SHAPM) Devices For Biochemical Sensors", 1996 ERDEC Conference On Chemical and Biochemical Detection (in press, <ftp://ftp.biode.com/erdec96.doc>).
 33. S. J. Martin, A. J. Ricco, T. M. Niemczyk and G. C. Frye, "Characterization of SH Acoustic Plate Mode Liquid Sensors", *Sensors & Actuators* 20 (1989) 253-268.
 34. E. Gizeli, N. Goddard, C. Lowe and A. Stevenson, "A Love Plate Biosensor Utilizing a Polymer Layer", *Sensors and Actuators B* 6 131-7 (1992).
 35. R.L. Baer, C.A. Flory, M. Tom-Moy and D.S. Solomon, "STW Chemical Sensors," *Proc. 1992 Ultrasonics Symp.*, pp. 293-298 (1991).
 - 36 Quartz crystals supplied by Maxtek, Inc., Torrance CA.

-
- 37 R. Smythe, "Crystal Filters", in Miniaturized and Integrated Filters, Mitra and Kurth, editors, pp. 280-328 (1989).
 38. Motorola, M68MPFB1632 User's Manual, *Motorola Literature Distribution, June, 1994.*
 39. Motorola, MC68HC916X1 Technical Summary, *Motorola Literature Distribution, 1996.*
 40. HIWARE, HI-CROSS V2.7 Reference and User's Manual, *Hiware AG, 1995*
 41. Optrex, LCD Liquid Crystal Display 1995, *Optrex Corporation, 1995, 81-87.*
 42. Grayhill, Keypad Data Sheet, *Grayhill 1996*
 43. National Semiconductor, MM74C923N 5x4 Keypad Encoder, *National Semiconductor Literature*
 44. Analog Devices, Octal 8-Bit CMOS D/A Converter DAC8800, *Analog Devices, Rev. A.*



DEPARTMENT OF THE ARMY
US ARMY MEDICAL RESEARCH AND MATERIEL COMMAND
504 SCOTT STREET
FORT DETRICK, MARYLAND 21702-5012

REPLY TO
ATTENTION OF:

MCMR-RMI-S (70-1y)

4 Dec 02

MEMORANDUM FOR Administrator, Defense Technical Information Center (DTIC-OCA), 8725 John J. Kingman Road, Fort Belvoir, VA 22060-6218


SUBJECT: Request Change in Distribution Statement

1. The U.S. Army Medical Research and Materiel Command has reexamined the need for the limitation assigned to technical reports written for this Command. Request the limited distribution statement for the enclosed accession numbers be changed to "Approved for public release; distribution unlimited." These reports should be released to the National Technical Information Service.

2. Point of contact for this request is Ms. Kristin Morrow at DSN 343-7327 or by e-mail at Kristin.Morrow@det.amedd.army.mil.

FOR THE COMMANDER:

Encl


PHYLIS M. RINEHART
Deputy Chief of Staff for
Information Management

ADB218773	ADB229914
ADB223531	ADB229497
ADB230017	ADB230947
ADB223528	ADB282209
ADB231930	ADB270846
ADB226038	ADB282266
ADB224296	ADB262442
ADB228898	ADB256670
ADB216077	
ADB218568	
ADB216713	
ADB216627	
ADB215717	
ADB218709	
ADB216942	
ADB216071	
ADB215736	
ADB216715	
ADB215485	
ADB215487	
ADB220304	
ADB215719	
ADB216072	
ADB222892	
ADB215914	
ADB222994	
ADB216066	
ADB217309	
ADB216726	
ADB216947	
ADB227451	
ADB229334	
ADB228982	
ADB227216	
ADB224877	
ADB224876	
ADB227768	
ADB228161	
ADB229442	
ADB230946	
ADB230047	
ADB225895	
ADB229467	
ADB224342	
ADB230950	
ADB227185	
ADB231856	